

Iron Quantum Dots Electro-Assembling on Vulcan XC-72R: Hydrogen Peroxide Generation for Space Applications

Armando Peña-Duarte,* Santosh H. Vijapur, Timothy D. Hall, Kathleen L. Hayes, Eduardo Larios-Rodríguez, Joselyn Del Pilar-Albaladejo, Mitk'El B. Santiago, Stephen Snyder, Jennings Taylor, and Carlos R. Cabrera*

Cite This: *ACS Appl. Mater. Interfaces* 2021, 13, 29585–29601

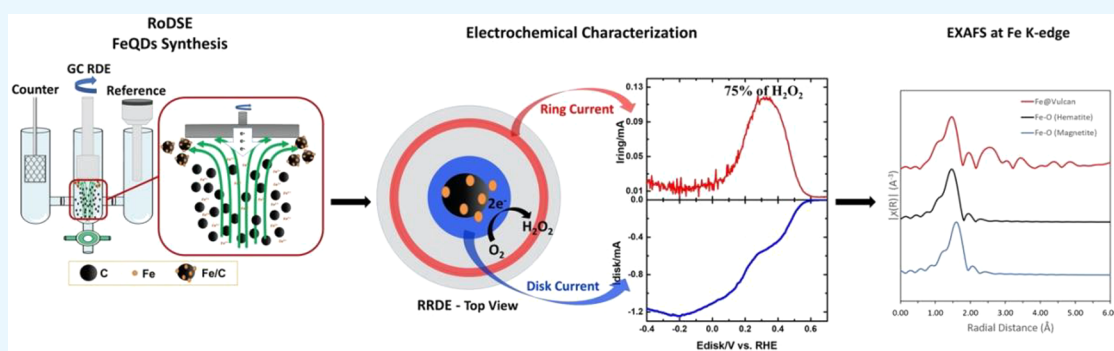
Read Online

ACCESS |

Metrics & More

Article Recommendations

Supporting Information



ABSTRACT: Highly dispersed iron-based quantum dots (QDs) onto powdered Vulcan XC-72R substrate were successfully electrodeposited by the rotating disk slurry electrodeposition (RoDSE) technique. Our findings through chemical physics characterization revealed that the continuous electron pathway interaction between the interface metal–carbon is controlled. The rotating ring-disk electrode (RRDE) and the prototype generation unit (PGU) of *in-situ* H₂O₂ generation in fuel cell experiments revealed a high activity for the oxygen reduction reaction (ORR) via two-electron pathway. These results establish the Fe/Vulcan catalyst at a competitive level for space and terrestrial new materials carriers, specifically for the *in-situ* H₂O₂ production. Transmission electron microscopy (TEM) analysis reveals the well-dispersed Fe-based quantum dots with a particle size of 4 nm. The structural and chemical-physical characterization through induced coupled plasma-optical emission spectroscopy (ICP-OES), transmission scanning electron microscopy (STEM), X-ray diffraction (XRD), Raman spectroscopy, X-ray photoelectron spectroscopy (XPS), and X-ray absorption spectroscopy (XAS); reveals that, under atmospheric conditions, our quantum dots system is a Fe^{2+/3+}/Fe³⁺ combination. The QDs oxidation state tunability was showed by the applied potential. The obtention of H₂O₂ under the compatibility conditions of the drinking water resources available in the International Space Station (ISS) enhances the applicability of this iron- and carbon-based materials for *in-situ* H₂O₂ production in future space scenarios. Terrestrial and space abundance of iron and carbon, combined with its low toxicity and high stability, consolidates this present work to be further extended for the large-scale production of Fe-based nanoparticles for several applications.

KEYWORDS: iron, Vulcan XC-72R, RoDSE, quantum dots, electrodeposition, oxygen reduction reaction, hydrogen peroxide, fuel cell

1. INTRODUCTION

Space and terrestrial technologies are at the cutting edge of new materials developments with ultrahigh performance in fuel cells, batteries, and supercapacitors applications.^{1,2} Desirable features such as high-power density production, high rate performance, high reliability, short loading time, cycling stability, and low maintenance costs are the main characteristics to be achieved in new energy-related devices. Several studies have been dedicated to creating new electrode materials, improving the specific capacitance and the operating voltage, while not sacrificing the power density and cycle life.^{2,3}

Among the electrochemical energy production devices, fuel cell-based technology has captured considerable attention

during recent years due to its distinctive clean production process. In fuel cells, the oxygen reduction reaction (ORR) is a determinant cathodic reaction.⁴ ORR can proceed by two pathways in aqueous electrolytes, an indirect 2-electrons pathway (Reaction 1) and a direct 4-electrons pathway

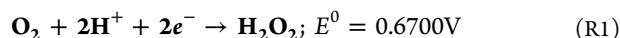
Received: March 26, 2021

Accepted: June 1, 2021

Published: June 17, 2021



(Reaction 2).⁵ For efficient production of energy in a fuel cell, ORR catalysts via 4-electrons route are to be carried out.⁶ Hydrogen peroxide is one of the most demanded compounds globally, and its production efforts have recently been aimed at scientific research.⁷ Simultaneously, a rising interest in *in-situ* H₂O₂ production for space applications has been developed.^{1,8}



Several electrochemical technologies are emerging to improve system sustainability, recyclability, and durability. One of those areas that require new materials carrier to achieve targeted lifetimes, efficiencies, and production rates are related to disinfecting solutions. Cleaning and sanitizing solutions against exposures to bacteria and viruses, such as the COVID-19, are increasingly further necessary to guarantee a sustainable, safe, and quality life in earth and space environments. The H₂O₂ disinfecting power represents a solution to sterilization processes within closed systems. Peroxide has nontoxic decomposition products (*viz.*, O₂ and H₂O), is safe for direct skin contact at functional active concentrations (~1–5% w/w),⁸ and has demonstrated disinfection capability.⁹

In addition, space missions cleaning requirements need to become autosustainable, allowing closed-loop living systems to be less dependent on earth resources. Direct *in-situ* electrochemical syntheses of H₂O₂, by optimizing the ORR catalyst via two-electrons process,¹⁰ represents an alternative to the current industrial production, avoiding unsafe and expensive transport procedures from earth. Hydrogen peroxide electrochemical synthesis is an attractive generation method because it requires no reactive precursors to be stocked, just supporting electrolytes to be combined to a suitable onboard water supply to form the feed solution for the device generation.^{1,8}

Recently, *in-situ* hydrogen peroxide production has been reported under terrestrial and zero-gravity flight experiments, through technology developed between Faraday Technology Inc. and the University of Puerto Rico.^{1,8} These experiments revealed no effect on the hydrogen peroxide generation performances under zero-gravity compared to ground experiments. Nevertheless, more developments on novel catalysts design are needed to improve the ORR efficiency toward peroxide. Accordingly, it is essential to evaluate the materials source spectrum, that is, its catalytic activity for ORR, its abundance, accessibility, and costs, even if they exist in terrestrial or extraterrestrial locations. Several physical and chemical processes on earth and space are based on carbon and iron compounds.¹¹ Carbon and iron are teaming in the known environments being explored by NASA. Moreover, the U.S. DOE Strategic Plan requirements of reliable, clean, and affordable energy science-driven technologies goes in the same direction.¹² Therefore, it is important to evaluate the successful use of iron- and carbon-based materials for ORR. The on-demand disinfectant system is an interesting adaptation of fuel cell gas diffusion cathode technology in combination with a suitable catalyst to promote an efficient two-electron reduction pathway to hydrogen peroxide. This system represents a technologic for the disinfecting process in space, specifically for the future Moon and Mars missions.¹

Iron-based materials have been broadly studied on behalf of iron ores abundance and their high catalytic efficiency. These catalysts further contribute to extending fuel cell lifetime by preventing cell degradation due to peroxide radicals.¹³ Iron

oxides have been synthesized via subsequent heat treatment by coprecipitation technique.¹⁴ Nevertheless, Fe₃O₄ and α -Fe₂O₃ particles often are in bulk sizes and are of low electrical conductivity. To improve the electrical properties and the performance of the superficial redox reactions between the active storage energy material and electrolyte, several researchers have focused on creating metal oxide on highly conductive nanocarbon composites.^{3,15} The electrical improvement is particularly important over the conduction requirements for the electrode–electrolyte interface in fuel cells, batteries, and supercapacitors.² Nanostructured iron- and carbon-based materials, oriented to energetic applications, have been synthesized via chemical vapor deposition technique (CVD). However, these systems generate iron nanoparticles covered and inactivated by carbon nanotubes and aerogels.¹⁶ Thermal processes have been used to produce iron–carbon composites but with insufficient amounts for large scale applications.³

In catalytic processes, the chemical activity is improved when nanosized structures are used.¹⁵ Appropriate experimental conditions allow obtaining low dimensional structures of different symmetries such as quantum dots (QDs).¹⁷ Although the semiconductor QDs are the most studied group, a QD is any solid in which all dimensions decrease to a few nanometers.¹⁸ The challenge to overcome it is to obtain a bulk production of highly dispersed iron-based QDs onto powdered carbon substrates, especially for *in-situ* H₂O₂ generation via ORR.^{1,8} Equally important, the interface metal–carbon must be controlled to ensure a continuous electron pathway between them. A novel and successful electrochemical method, known as the rotating disk slurry electrodeposition technique (RoDSE),¹⁹ have been applied to deposit metal nanoparticles on different support materials for bulk production of catalyst powder.^{15,19,20} In RoDSE, a circular flux of solution occur by means of the working electrode rotation. Flux is maintaining constant, replacing continuously the concentration of carbon nanostructures and metallic ions in the diffusion layer, allowing the electrodeposition of the metal to take place at the carbonaceous support.²⁰ Nanostructures prepared by the RoDSE technique produce bulk quantities of carbon-supported nanocatalysts while also avoiding agglomerations of the nanoparticles.¹⁵

In our study, a large-scale electro-assembly of highly dispersed iron-based QDs onto powdered Vulcan XC-72R is presented via RoDSE technique, without high temperatures nor hazardous compounds. Our findings, through physical chemical characterization, revealed that 4 nm iron-based quantum dots were successfully electrodeposited on Vulcan XC-72R. The electrochemical results showed a continuous electron pathway interaction between the interface metal–carbon, controlled by the tunable Fe oxidation state. The ORR properties and H₂O₂ production in KOH and deionized (DI) water were shown by the Koutecky–Levich (K-L) kinetics analysis of rotating disk electrode (RDE) polarization curves, rotating ring-disk electrode (RRDE) technique, and *in-situ* H₂O₂ generation experiments.

2. EXPERIMENTAL SETUP

2.1. Electrochemical Techniques. Iron Nucleation and Electrodeposition on Glassy Carbon Electrode (GCE). In order to determine the characteristic potentials, such as deposition potential, the onset of hydrogen reduction reaction, and the onset of anodic oxidation, cyclic voltammetry (CV) experiments were done. The CVs

were done as follows: (1) A clean glassy carbon electrode was immersed in a 5 mM $\text{FeCl}_3/0.1$ M KClO_4 solution stored in a capped three-way cell. Reversible hydrogen electrode (RHE) and Pt wire were used as reference and counter electrodes, respectively. (2) The electrochemical measurements were done using a Biologic SP200s Potentiostat/Galvanostat Electrochemical Workstation. (3) The solution was bubbled with nitrogen during 15 min to remove dissolved oxygen prior to CV measurement. (4) To study Fe nucleation progression and the GCE surface modification during the electrodeposition process, CV analysis was done continuously through the process. A total of 49 potential cycles were carried out using a potential window between 0.5 V and -0.9 V vs RHE and a potential scan rate of 10 mV/s.

Electrodeposition of Iron Based Quantum Dots on Vulcan XC-72R by the RoDSE Technique. Iron nanoparticles were electrodeposited on Vulcan XC-72R (from CABOT) carbon support by the RoDSE technique¹⁹ at an applied potential of -855 mV vs RHE (see Supporting Information (SI) Figure S1). This applied potential was selected from CV studies. The RDE was a glassy carbon electrode with a geometric area of 0.20 cm² and was previously polished in an eight-pattern movement on felt pads with 1.0, 0.3, and 0.05 μm aluminum oxide (Buehler Micropolish). The RDE was rinsed with DI water and sonicated during 10 min in ethanol to ensure alumina residue was removed. A high surface area Pt-mesh and a RHE were used as a counter and reference electrodes, respectively. A slurry suspension was prepared by suspending 20 mg of Vulcan XC-72R in 20 mL of 0.1 M KClO_4 solution, and it was maintained under ultrasound for 1 h. The highly dispersed slurry suspension was poured to the centered compartment of a three-electrode cell assembly as shown in SI Figure S1. The other two cells, separated by sintered glass frits, were filled with 20 mL of 0.1 M KClO_4 . Finally, the total volume of each chamber was completed until 25 mL with the electrolyte. Subsequently, 2 mL of 5.0 mM FeCl_3 solution, the metallic nanoparticles precursor, were added into the carbon slurry. The settled suspension was mixed by rotating the RDE at 2400 rpm and bubbling vigorously with ultrahigh purity nitrogen for 15 min. Then, an electrodeposition potential of -855 mV vs RHE was applied for 1 h. After finishing the chronoamperometry process, three additional aliquots of 2 mL were added, which are elapsed in 2 h periods each of electrodeposition. The resulting iron-based catalyst slurry material was filtered through a 0.22 mm Nylon membrane and washed with 1000 and 20 mL of DI water and pure ethanol, respectively. Samples were dried in a desiccator for 24 h and physically ground in an agate mortar to obtain a homogenized powder.

Electrochemical Characterization. Catalytic performance characterization was done using Fe catalyst inks modified glassy carbon electrodes. Iron based catalyst inks were prepared by mixing 1 mg of catalyst powder with 50 mL of DI water, 50 μL of isopropanol, 150 μL of ethanol and 20 μL of Nafion solution (5% perfluorinated resin in ethanol from Aldrich). The mixture was placed under ultrasound for 1 h to form a homogeneous suspension. Afterward, 3 mL of the prepared catalyst ink were dropped cast on a cleaned glassy carbon surface and was dried at room temperature for 15 min. CV experiments were done in 0.1 M KOH solution using a potential window of -0.4 to 1.2 V vs RHE. Oxygen reduction reaction (ORR) activity measurements were done with a glassy carbon rotating disk electrode (RDE) between 1.0 V and -0.3 V vs RHE. The Koutechy–Levich (K–L)²¹ analysis was done in O_2 -saturated 0.1 M KOH solution at a scan rate of 10 mV/s at rotation speeds between 400 and 2400 rpm. The hydrodynamic rotating ring disk electrode (RRDE) analysis was completed by running the Fe/Vulcan modified glassy carbon disk and a Pt ring in KOH 0.1 M. The potential was swept between 1.0 and -0.4 V vs RHE at a scan rate of 10 mV/s. The ring potential was fixed at 1.20 V vs RHE and the electrode rotation rate applied was set at 1600 rpm.

2.2. Structural and Chemical–Physical Properties. Induced Coupled Plasma–Optical Emission Spectroscopy (ICP–OES) and Metal Loading. The iron-based catalysts metal loading was determined using an Optima 8000 PerkinElmer ICP–OES. For ICP–OES analysis, 10 mg of each iron-based catalyst were digested with 10

mL of a nitric acid and hydrochloric acid solution at a 1:3 molar ratio. This mixture was heated until boiled gently and the solution volume was reduced to 1 mL. The obtained solutions were filtered through a Whatman glass microfiber filter (GF/F grade) and quantitatively diluted with 2% HNO_3 in volumetric flasks. The iron concentration was determined by triplicates quantitative analysis.

Transmission Electron Microscopy (TEM), Transmission Scanning Electron Microscopy (STEM) and the High-Angle Annular Dark-Field Scanning Transmission Electron Microscopy (HAADF–STEM, Contrast–Z). The electron micrographs were obtained using an FEI Tecnai F20 G2 equipped with X-ray fluorescence-energy dispersive spectrometry (EDS) system, operated with an accelerating voltage of 200 kV and an Oxford X-Max detector. This was done at the Cornell Center for Materials Research Shared Facilities. The TEM analysis samples were prepared by placing a drop of dispersed catalyst onto the carbon-coated copper grid and dried at room temperature. EDS was used to analyze the elemental composition of the catalyst.

X-ray Diffraction (XRD) Measurements. Iron-based catalyst synthesized via the RoDSE technique were characterized by X-ray diffraction (XRD) using a RIGAKU SmartLab X-ray diffractometer. Experiments were done in reflectance Bragg–Brentano geometry, working with a Cu $K\alpha$ radiation source of $\lambda = 1.5406$ Å. An X-ray tube current was 44 mA and an applied voltage of 40 kV. The diffractometer was equipped with a high-speed ID detector (D/teX Ultra).

Raman Scattering. Raman characterization was done to study the chemical functionalities of the pristine carbon support and the iron-based carbons prepared by the RoDSE technique. Raman spectra were determined at room temperature, using a Thermo Scientific DXR Raman Microscope with a laser wavelength of 532 nm. Wavelengths between 100 and 3000 cm^{-1} were measured. The laser power was placed at 5.0 mW in order to avoid sample modification or degradation. The measurement error was ± 2 cm^{-1} .

Surface Analysis by X-ray Photoelectron Spectroscopy (XPS). XPS was used in order to determine the chemical composition of iron-based catalysts surface. XPS spectra were done by means of a PHI 5600ci spectrometer, with an Al $K\alpha$ polychromatic X-ray source of 350 W settled at 45° and a hemispherical electron energy analyzer. The 500 μm X-ray spot aperture was used for XPS analysis. Pressure in the ultrahigh vacuum analysis chamber was below 9×10^{-9} mbar. Carbon tapes were used as adhesive support of small quantities of the iron-based catalytic and Vulcan samples. Survey spectra and high-resolution spectra for Fe 2p, C 1s, and O 1s XPS binding energy regions were recorded. The results were deconvoluted and analyzed using Multipack Physical Electronics curve-fitting program. The binding energy was correct by the C 1s peak at 284.5 eV.

X-ray Absorption Spectroscopy (XAS). XAS experiments were carried out at the beamline for materials measurements (BMM) 6-BM at the National Synchrotron Light Source II (NSLS II) in Brookhaven National Laboratory. The energy of the absorption spectra was calibrated using a Fe metal foil. The sample was prepared by grinding the solid until obtaining a fine powder. The powder was then evenly spread on a Kapton tape until achieving a homogeneous film. The Fe K-edge absorption spectra was collected in transmission mode and later analyzed using the DEMETER program package and following standard procedures described elsewhere.²² Crystal information files PDF 01–072–6226 (hematite) and PDF 01–080–6402 (magnetite), obtained from the ICDD PDF4+ database, were used to calculate scattering paths during extended X-ray absorption fine structure (EXAFS) analysis.

2.3. In-situ Electrochemical Hydrogen Peroxide Generation for Space Applications. The hydrogen peroxide generation study on Fe/Vulcan catalyst and gas diffusion electrode (GDE)-microporous layer (MPL) was done at 4, 6, 8, 10, 12, and 14 V. The catalyst sample was dispersed in an ethanol:isopropanol:water (1:1:2) mixture with a total solution volume of 750 and 60 μL of Nafion solution 5% in ethanol. Dispersions were painted onto a new GDE–MPL. Differential polarization tests were done at a single pass system. CeTech carbon cloth GDE–MPL were used as electrodes. A flow rate of 2 mL/min of reverse osmosis (RO) water was applied through the

catholyte plate, with a thickness of 0.37". The pressure balance was kept at 1 psi. The electrolyte was a mixture of Nafion NR 50 Beads and POWDion-Insoluble, 40–60 mesh. The Nafion blend was activated at 80 °C in successive steps as follow: 3% H₂O₂ for 1 h, DI water for 2 h, 1 M H₂SO₄; and stored in DI water. Fe/Vulcan and the GDE-MPL polarization curves were done to determine the *in-situ* hydrogen peroxide generation at Fe/Vulcan and GDE. In addition, the output current and the H₂O₂ w/w%, as a discrete potential function, was determined for each trial.

3. RESULTS AND DISCUSSION

3.1. Iron Nucleation, Electrodeposition Potential Determination, and Nucleation Evolution on Glassy Carbon Electrode (GCE). *Nucleation process by cyclic voltammetry:* in order to determine the characteristic Fe redox potentials, such as Fe deposition potential, the onset of the hydrogen reduction reaction, and the onset of anodic oxidation, a cyclic voltammetry experiment set was done using a RHE and a Pt wire as reference and counter electrodes, respectively. Figure 1 shows the cyclic voltammetry plot of a cleaned glassy carbon working electrode immersed in a nitrogen-purged 5 mM FeCl₃ and 0.1 M KClO₄ solution. A starting potential of 0.5 V vs RHE was chosen to ensure that both iron species, Fe²⁺, on the near surface, and Fe³⁺, in the bulk solution, were present. A potential scan rate of 10 mV/s was applied between 0.5 V and −0.9 V vs RHE. The CV closely resembles previously reported cyclic voltammetry for iron-based chunks and bulk materials in different electrolytes.^{23,24}

The crossovers of the current curves in the cathodic and anodic branches occurs due to the difference in deposition and dissolution potentials and can be due to nucleation and growth of metallic iron. This behavior is associated with reversible systems which involve undissolved species. The presence of a crossover is a diagnostic for the nuclei formation on the electrode.^{25,26} The pH of the 5 mM FeCl₃ in 0.1 M KClO₄ solution was 4.07 ± 0.01, which implies that ionized iron species would prefer to exist as ferrous and ferric ions, rather than complex with anionic species of electrolyte.²⁷ However, the wavy and ill-defined I_c and I_{2c} cathodic peaks, shown in Figure 1, could indicate that reduction–oxidation pathway of iron involves the formation of hydroxides species²⁴ in slight quantities. The cathodic current region evaluation in Figure 1, reveals the I_c and I_{2c} current density peaks which can correspond to Fe³⁺ to Fe⁰ and Fe³⁺ to Fe²⁺ to Fe⁰ reduction processes and, as well as, to Fe(OH)_x to Fe⁰ reduction.^{24,27,28} Meanwhile, I_{3c} could be assigned to the Fe²⁺ to Fe⁰ reduction process.²⁹

Peaks I_c and I_{2c} can correspond to the reduction of FeOOH species to Fe(OH)₂, which have been previously reported in saline electrolytes and oxygen-free atmosphere.²⁹ Iron complexes, containing both Fe²⁺ and Fe³⁺ species, will be formed near the electrode at the applied electrodeposition conditions. Based on the Pourbaix E-pH equilibrium diagram of the aqueous iron/chloride system at 25 °C, the simultaneous presence of ferrous and ferric dissolved species is expected at the electrode interface.³⁰ The resulting positive iron complexes are compensated with perchlorate and chloride anions, that usually are in the outer-sphere complex in diluted solutions.³¹ I_a current peak is associated with oxidation processes of adsorbed hydrogen.²⁹ The following current peaks, I_{2a} and I_{3a}, are produced whether as a corrosion product of Fe⁰, through oxidation of an initial ferrous hydroxide layer, or by direct iron oxides precipitation in the

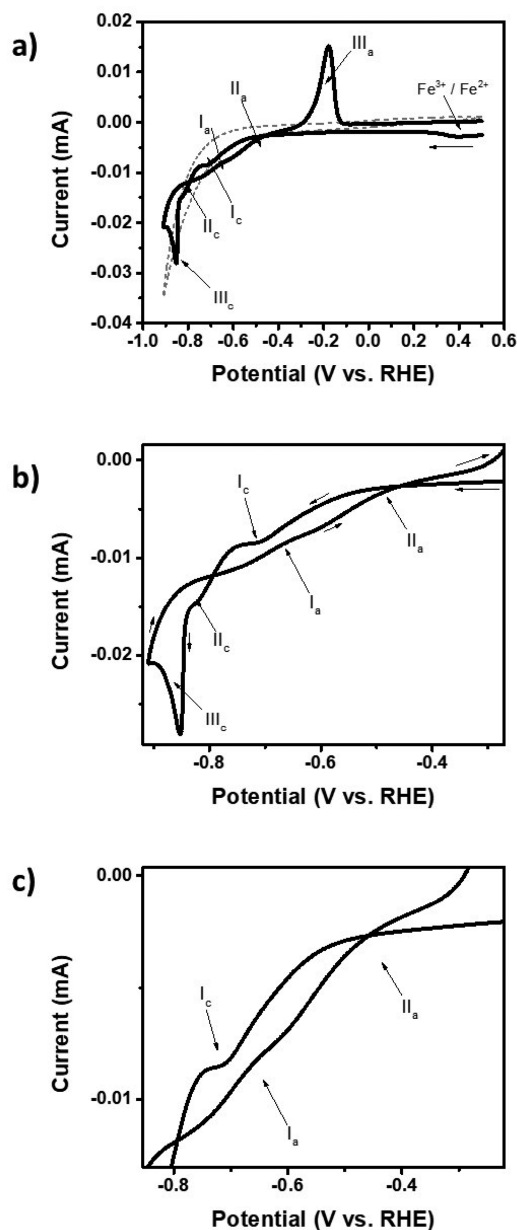


Figure 1. Cyclic voltammetry of Fe³⁺ at a GCE, at a scan rate of 10 mV/s and at room temperature. The first cyclic voltammogram (a) in 0.1 M KClO₄ (dashed gray line) and in a 5 mM FeCl₃/0.1 M KClO₄ solution (solid black line). Enlarged views of the potential windows (b) between −0.9 V and −0.3 V vs RHE oxidation and (c) and between −0.85 V and −0.2 V vs RHE are shown below.

simultaneous presence of Fe²⁺ and Fe³⁺ species. As we mentioned above, the CVs interpretation and peaks position attribution were based on the iron electrochemistry previously reported in the literature.^{24,27,28} However, the aim of this CV analysis was to determine the iron electrodeposition potential to produce iron nanoparticles on carbon substrates. An in-depth analysis is required to characterize all the iron species involved in the redox processes at the selected potential window.

Iron Nucleation Process at GCE. To study the Fe nucleation at the GC electrode surface, during the metallic iron electrodeposition, cyclic voltammetry analysis was done at different stages of the process (see Figure 2). A total of 49 potential cycles were done between 0.5 V and −0.9 V vs RHE

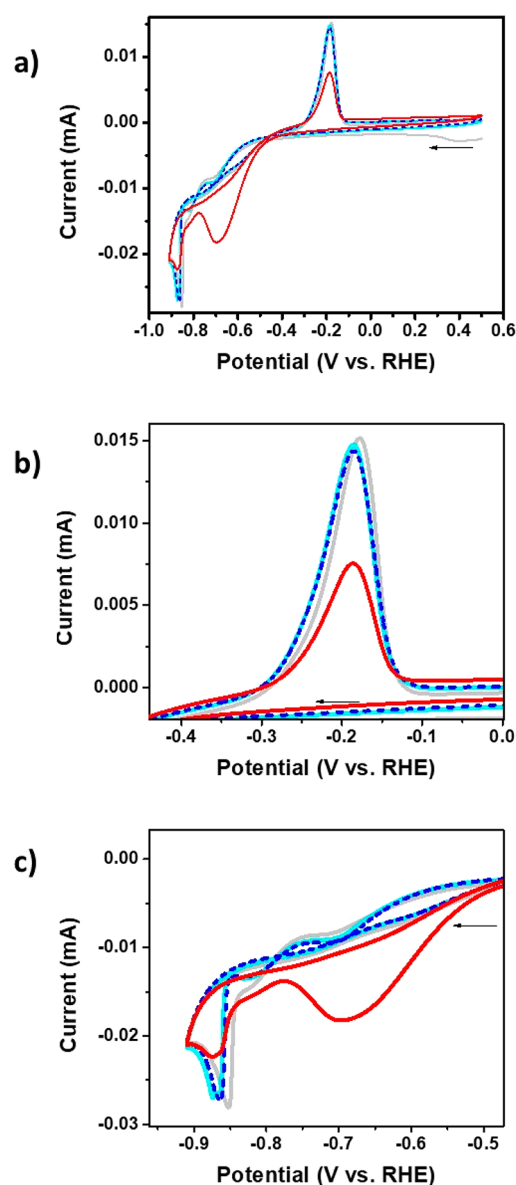


Figure 2. (a) Cyclic voltammograms profiles vs RHE, at a scan rate of 10 mV/s and at room temperature, of a glassy carbon electrode immersed in a 5 mM FeCl_3 /0.1 M KClO_4 solution. The deviation of the first cycle (solid gray line), from the successive 2 (solid light blue line), 3 (dashed dark blue line), and 49 cycles (solid red line), is observed in both reduction and oxidation peaks. The potential is swept in the cathodic direction starting at 0.5 V and ending at -0.9 V. Enlarged views of the (b) oxidation and (c) reduction peaks are shown below.

and by using a potential scan rate of 10 mV/s. As shown in Figure 2, a distinctive increase of the cathodic and anodic peak currents occurs as a function of potential cycle number. Only cycles 1, 2, 3, and 49 are presented in Figure 2. The iron electrodeposition CV displays the characteristic iron cathodic and anodic peaks as was explained above, with remarkable changes in peak current and shape which are due to the growth on the electrodeposited iron (see Figure 2). The CV experiments showed reproducibility after three replications. In the anodic potential scan, the oxidation peaks Ia, IIa, and IIIa were similar to those shown in Figure 1. Peaks Ia and IIa disappear after a few cycles; on the contrary, IIIa increases notably its current peak intensity until the second cycle, then it

starts to decrease. The slow decrease of the deposition peak IIIc intensity indicates that the formation of the nanoparticles is a limiting step on the electrochemical process. Moreover, the reduction peak IIIc decreases as the iron concentration changes over time. The iron deposition occurs slowly in 0.1 M KClO_4 electrolyte, allowing the formation of very small nanostructures. The current performance differences, from the second cycle onward, is due to iron nanoparticles or film formation, which form in the first cycle on glassy carbon electrode surface. The following iron deposition occurs on two surfaces, the active iron-based sites formed at the electrode surface and on the free GC surface that coexist during the earliest cyclic periods.

Based on the sharp shaped of the iron reduction peak IIIc (see Figure 1), the maximum current electrodeposition peak at -855 mV vs RHE was selected for the RoDSE iron deposition on Vulcan XC-72R carbon support. However, even though -855 mV vs RHE is the Fe^{2+} to Fe^0 redox potential—based on the Figure 1 and the iron E vs pH Pourbaix diagram—depolarization of metal deposition can result as a consequence of carbon flakes presence in the slurry suspension during the RoDSE process.^{15,20}

3.2. Iron Quantum Dots (FeQDs) Electrodeposition onto Vulcan XC-72R by the RoDSE Technique. Chronoamperometric Electrodeposition. Prior to the Fe electrodeposition, 1 h ultrasonic treatment followed by electrode rotation under open circuit, at 2400 rpm for 5 min in the presence of N_2 , were critical to have a good carbon support distribution through a controlled and constant hydrodynamic flux, achieving a highly homogeneous slurry system. Well-distributed precursor support enhances the probability that whole Vulcan particles can collide with the RDE surface, decreasing the effect of heterogeneous accumulation of carbon in some parts more than in other cell regions. The chronoamperometry profile related to the iron electrodeposition behavioral process onto the carbonaceous matrix is shown in Figure 3. Specifically, an electrodeposition potential of -855 mV vs RHE was applied to the RoDSE glassy carbon electrode while under a 5 mM FeCl_3 in 0.1 M KClO_4 solution mixed with Vulcan XC-72R. These

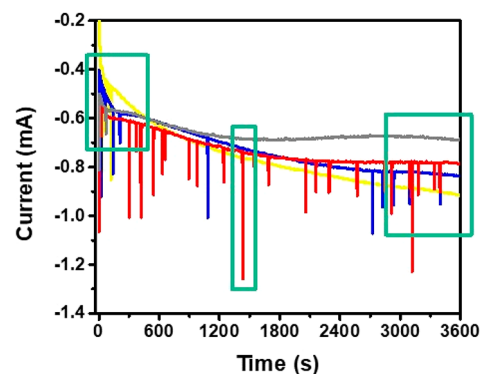


Figure 3. Chronoamperometry RoDSE profile for the iron electrodeposition onto Vulcan XC-72R. Current profiles for the FeQDs/C catalyst were obtained in 20.0 mg of carbonaceous matrix in 20.0 mL of 0.1 M KClO_4 slurry. A glassy carbon RDE, at a rotating speed of 1900 rpm and an applied potential of -0.855 V vs RHE, were used. The chronoamperometric process was repeated three additional times with the addition of 2.00 mL aliquots of 5 mM FeCl_3 in each repetition: aliquot 1 (yellow line), aliquot 2 (blue line), aliquot 3 (red line), and aliquot 4 (gray line).

control parameters were done four times per consecutive 2.00 mL aliquot addition of 5 mM FeCl₃, after 1 h electrodeposition periods.

The iron concentration in the slurry solution was the variable from what cathodic currents depend. It was found that for each added 2 mL-aliquot of iron solution precursor, as is shown in Figure 3, the average deposition current decreased with time. The current decrease with deposition time can be explained by the Fe concentration reduction in the solution.^{15,20} Profiles of each added aliquot revealed the characteristic current–time chronoamperograms, in which the current is decreasing as a function of electrodeposition time until a quasi-plateau is reached. This current vs time curve performance is slightly similar to a characteristic instantaneous nucleation growth.¹⁵ First, a small and sudden change in the current appears at ca. 20 s, that is, a small current widespread peak was observed in the cathodic current for all the aliquot chronoamperometric plots. This change corresponds to an induction period of iron nucleation on the glassy carbon electrode or on the unsupported carbon matrix used in RoDSE. Second, the rate of mass transfer around the particle, nucleation of iron on Vulcan or onto the glassy carbon electrode, and the addition of the hydrogen evolution current could explain the exponential current increase until passing a mean of 200 s. Finally, the Fe³⁺ concentration decreases in solution, while under RoDSE conditions, and a quasi-plateau is reached due to the hydrogen evolution.

Iron precursor aliquots addition provokes a modest increase in the currents during the first seconds of the electrodeposition process. Hydrogen evolution is responsible for the randomly current density patterns observed in Figure 3.²⁴ Potassium perchlorate as electrolyte solution guarantees that iron ions must be stable as Fe-complex instead of precipitated species, as well as, avoids the creation of new functionalities on the carbon support. This ensures a lack of new oxygen functionalities in the Vulcan matrix. Only changes as a function of applied potential can be evaluated.

Iron-based QDs electro-formation occurs due to the hydrodynamic flow, generated by the RDE, drawing all the components inside the cell to an infinitesimal distance of the glassy carbon surface. Therefore, in the radial vicinity of the electrode, a laminar, stable, and continuous flow is created, in which redox processes are developed in microscopic dimensions. There are three possible end-ways of the iron reduced species. First, it could be deposited on the glassy carbon electrode surface. Second, iron QDs could be formed and drift freely in the slurry. Finally, and the major expected pathway to arrange an iron–carbon catalyst, iron is deposited on Vulcan. Stiff and sharp current peaks observed in the chronoamperograms (see Figure 3) can be due to iron nanostructures deposited or not on Vulcan, hitting the RDE glassy carbon surface. These chronoamperometric current peaks are signs that solid iron composites have been grown. Iron-based quantum dots catalysts formed, rusty once they are in contact with the solution, are electrochemically reduced when their random Brownian motion results in a collision with the surface of the RDE.³²

In the RoDSE technique as a hydrodynamic method, where the diffusion layer is imposed by convection, the heterogeneous electron transfer kinetics and the electrochemical determination of transitional charged species are governed by an infinitesimal temporal resolution regime. The characteristic time scale $t_{\text{characteristic}}$ is derived using $t_{\text{characteristic}} = Ad^2D^{-1}$,

where A is a proportionality parameter that depends on the technique, and D is the diffusion coefficient.³³ The size of a stationary diffusion layer d is controlled by each technique. In this sense, in order to evaluate the transient currents generated in the RoDSE technique, it is possible to establish analogies with methods such as the ones use in micro- and nano-electrodes in the steady-state, and the scanning electrochemical microscopy technique. In these methods, the double layer charging currents do not interfere with the electrochemical measurements,^{33,34} and the collision transient currents could be determined through experiments carried out under controlled flow conditions.³⁵

The origin of the current transients could be associated with three processes: catalytic current induced by catalyst structure that generated the transient, the Fe-Vulcan and H₂O/H⁺ couple interaction through electrocatalytic amplification (ECA), and the direct electrochemical redox reaction of oxidized quantum dots themselves. QDs could be previously rusted on de Vulcan surface or by forming in solution iron/iron-oxides core–shell structures.^{36,37} The iron presence increases the amplification using the stochastic electrochemical techniques.^{34,38} The surface energy associate with the small-particle-size of the iron QDs synthesized and the negative values of enthalpy, Gibbs energies of formation, and standard entropy associates with the iron corrosion process in aqueous solution; enhances the probability to obtain iron structures with oxidized surface shells.

Forced convection applied during the RoDSE process increases the collision frequency dramatically.³⁹ The spiky-responses of the current–time profile that are shown in Figure 3 could be determined by the interaction between Fe-Vulcan catalyst and the electrode surface, QDs-Vulcan aggregate shape and size, iron quantum dots concentration, the diffusion coefficient of reactant in the whole slurry, the surface state of the glassy carbon RDE, the residence time of the nanoparticle on the electrode, and the applied potential.³⁶ This last variable is of remarkable importance in the studied system because, as was explained above (see Figure 1), at -855 mV iron electrodeposition, water reduction and hydrogen evolution process occur simultaneously.

During the first chronoamperometric seconds of each aliquot, the peaks could be generated by the higher iron ions concentration in the environment of the electrode after gathering aliquots.^{15,19,20,40} After adding the second aliquot, the frequency and intensity of spikes are determined by the production of iron nanostructures, and by the inhibition of hydrogen evolution by chloride concentration increment with aliquots addition. As an overview, the electron transfer may occur during the condensed time scale of the particle-electrode collisions,⁴¹ and the transient current peaks could be associate with the hydrogen coevolution on the iron-base quantum dots surface.⁴²

FeQDs/Vulcan Characterization by Cyclic Voltammetry. cyclic voltammetry analysis of the electrochemically synthesized iron-based catalyst supported on Vulcan XC-72R, via RoDSE technique, was done in a nitrogen-purged 0.1 M KOH solution. Figure 4 shows the cathodic–anodic-pair peaks which are associated with the superficial Fe³⁺/Fe²⁺ redox process of the iron oxides and hydroxides external layers. Notable differences appear by contrasting the current profiles shown in Figure 4 with the iron electrodeposition on the glassy carbon electrode shown in Figure 1. These differences are associated with a nanoscopic distribution of a determined

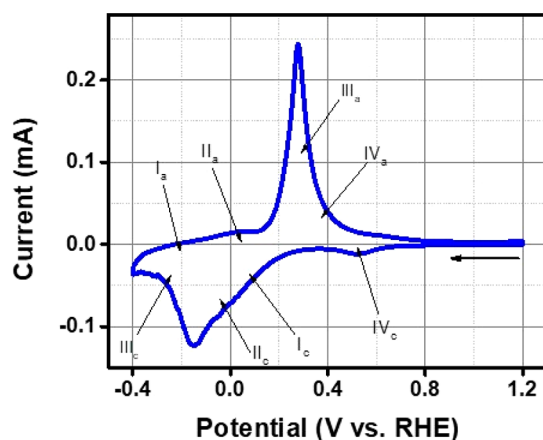


Figure 4. First cycle of the cyclic voltammetry analysis of the electrochemically synthesized iron-based catalyst supported on Vulcan XC-72R, via the RoDSE technique. CV analysis was done in a nitrogen-purged 0.1 M KOH solution. Characteristic cathodic and anodic peaks of Fe species are displayed in the voltammogram. Potential scan rate was 10 mV/s.

material onto another different solid. Moreover, the electrolyte and porosity-surface textural properties, are determinant factors in the resultant current peak shapes. Peak asymmetry and small current bumps in Figure 4 may suggest a contribution or convolution⁴³ of current peaks, for example, at the potential window used in this work some iron-based electrochemical processes^{23,24,27–29} can take place simultaneously. We encourage an in-depth cyclic voltammetry analysis of iron, as well as a deconvolution of current Gaussian peaks which could be associated with some redox changes.⁴³ However, comparing the CV in Figure 4 with the CVs reported in the literature for bulk iron structures^{23,24} and iron electrochemistry,^{24,27–29} the regions I_c, II_c, III_c, IV_c, I_a, II_a, III_a, and IV_a were delimited as possible voltage regions for iron current peaks. Regions I_c and II_c may correspond to the reduction processes of Fe³⁺ to Fe⁰ and Fe³⁺ to Fe²⁺ to Fe⁰. Also, FeOOH species may be formed and reduced to Fe(OH)₂. Region III_c may be assigned to Fe²⁺ to Fe⁰ reduction. Analyzing in the backward potential sweep direction, the regions I_a, II_a, and III_a were delimited. Region I_a is nearly imperceptible in the CV and it is commonly associated with the oxidation of adsorbed hydrogen.^{29,44} Region II_a is associated with the Fe⁰ to Fe²⁺ oxides and hydroxide species oxidation. Region III_a is attributed to possible processes such as the Fe(OH)₂ to Fe³⁺ species, to iron(III) oxides and oxyhydroxides electrooxidation.²⁹

Simultaneous presence of ferrous and ferric species is expected since iron oxides formation during the synthesis, by exposition to the atmosphere in postsynthesis treatments, and through interaction with the hydroxide ions which constitute the electrolyte. At the IV_a region, a possible inner iron(II) oxide layer could be oxidized to iron(III) oxide.²³

The alkalinity of the 0.1 M KOH solution, with a pH of 13, implies that hydroxide ions attack the iron-based catalyst. The cathodic region IV_c could be associated with the reduction of corrosion compounds⁴⁵ that are accumulated on the catalyst surface. The iron hydroxide compounds precipitation could be favored by the particle size effect when iron-based QDs are in contact with the strong alkaline anions of the electrolyte.

In the second cycle, shown in SI Figure S2, sharpness and well-definition of the cathodic–anodic-pair peaks are associ-

ated with superficial Fe³⁺/Fe²⁺ redox process on external layers of iron oxide or hydroxide. The diffusion phenomena of alkaline electrolytes through the catalyst have been solved after the first cycle. In a second scanning, the current peak intensity increase, indicating that the reaction occurs in a progression as the redox process drills the porous structures. After the electrochemical first sweep a more ordered structure of iron oxide and hydroxides are obtained (see SI Figure S3). Confinement effect accelerates the definition and sharpness of these peaks, if they are compared with the CVs obtained for bulk iron structures.^{23,24} Clearly, distribution on a conductive carbonaceous substrate influence remarkably in the current profile behavior. The interpretation of Figure 4 and SI Figure S3 is based on the iron electrochemistry previously reported in the literature^{24,27–29} However, as we mentioned above, an in-depth iron CV analysis is required to characterize all the iron species involved in the redox processes at the potential window scanned. Instead, we just determine the iron presence on the catalyst's surface through a CV scanning, we aimed our work to the structural, physicochemical, and the ORR catalytic properties characterization of our materials.

3.3. Structural and Chemical–physical Properties. Induced Coupled Plasma–Optical Emission Spectroscopy (ICP–OES) and Metal Loading. The quantitative determination of the total iron electrodeposited and its percentage ratio loading efficiency by the RoDSE technique were done through ICP–OES. As is shown in SI Table S1, 15.54% of iron by mass was deposited on the surface onto the surface of Vulcan XC-72R. Comparing this value with the 25.00% of iron by mass, to be theoretically loaded as the precursor of Fe nanoparticles, the electrodeposition efficiency was 62.16% per mass. These results agree with the iron presence reported above by cyclic voltammetry and HRTEM analysis, as it was similar in composition and distribution of Fe onto de carbon support surface. These results validate the RoDSE process applied, in views to fabricate nanostructured and powdered iron-based carbon catalysts with a high loading of iron. The iron loading higher than 60 percent is a noteworthy quantity of electrodeposited metal if it takes into consideration the constant competition between the simultaneous processes of water/protons reduction, iron nucleation, and the continuous molecular hydrogen bubbles evolution.

Transmission Electron Microscopy (TEM) and Scanning Transmission Electron Microscopy (STEM). Details of the electrodeposited catalyst's structure were obtained TEM and STEM, as is shown in Figure 5. Micrographs confirm the effectiveness of the RoDSE technique concerning the size, shape, and dispersion of the iron nanostructures onto the Vulcan XC-72R carbon support. TEM and STEM images recorder for Vulcan-support show the branched-nanochains of Vulcan particles, with the nanosized structures between 30 and 50 nm of diameter. Figure 5a (TEM) and Figure 5b (HRTEM) shows the Vulcan structure like cabbage, which works as anchoring support for metal nanoparticles. In Figure 5d (TEM) and Figure 5e (HRTEM) images of Fe/Vulcan catalyst supported on Vulcan are shown, where the metal-based nanoparticles were presented as dark spots on a lighter background of the carbon support. High-angle annular dark-field scanning transmission electron microscopy (HAADF-STEM) (Contrast-Z) are shown in Figure 5c,f. The elemental composition examined by the energy dispersive X-ray spectroscopy (EDS) analysis evidence the presence of iron (Figure 5g). HRTEM micrograph in Figure 5d shows the well-

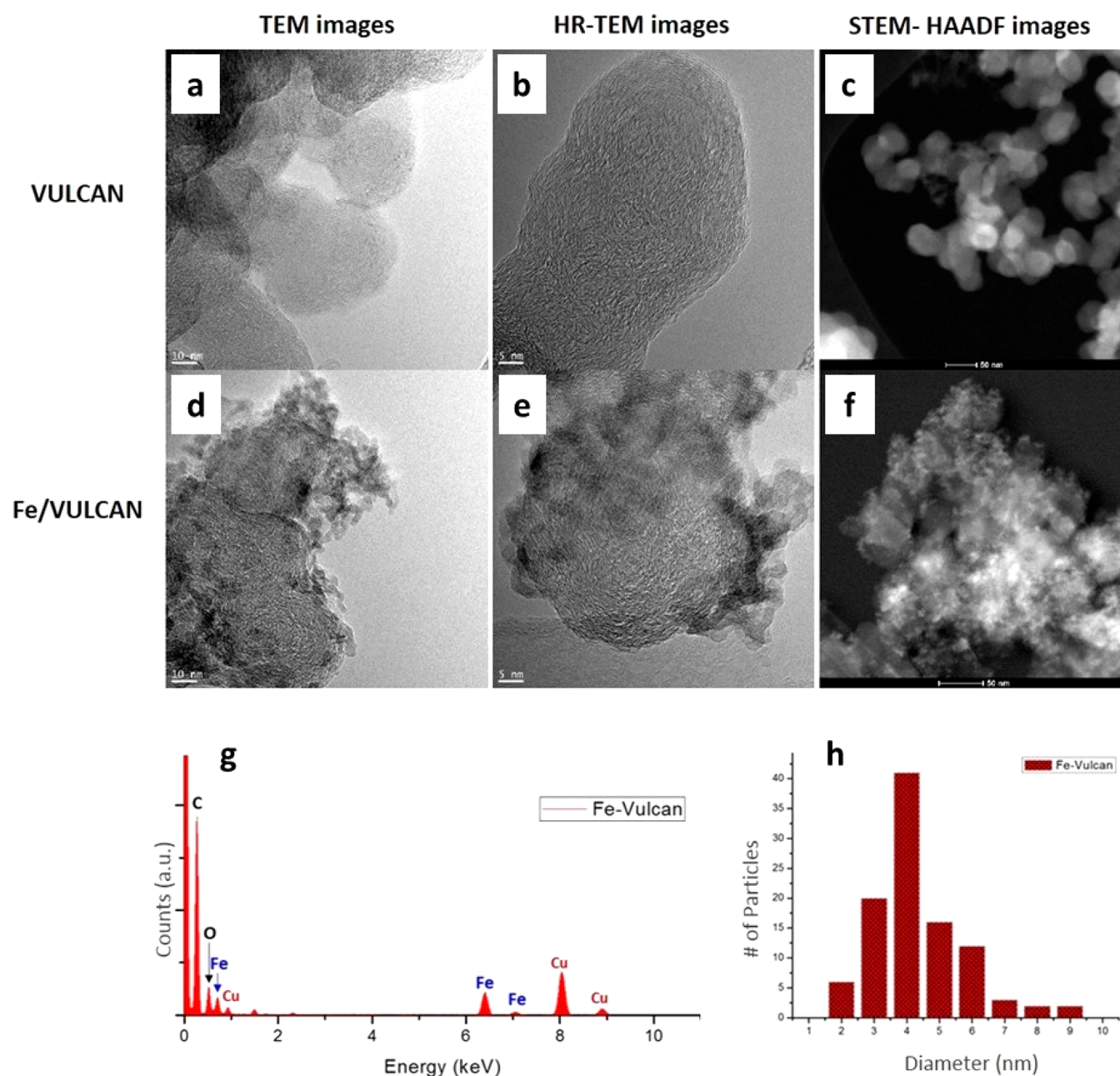


Figure 5. Transmission electron microscopy (TEM) (a,d), high resolution transmission electron microscopy (HR-TEM) (b,e), and high-angle annular dark-field scanning transmission electron microscopy (HAADF-STEM) (Contrast-Z) (c,f), of Vulcan and the Fe/Vulcan catalyst electrodeposited by the RoDSE technique. The energy dispersive X-ray spectroscopy (EDS) analysis evidence the presence of iron (g). The particle size histogram shows a narrow size distribution about 4 nm of Fe-based QDs onto Vulcan (h).

dispersed Fe quantum dots with a particle size of 4 nm. The narrow iron nanoparticle size distribution between 2 and 6 nm, mainly, is summarized in the histogram in Figure 5h. The narrow distribution below 10 nm and the semiconductor iron oxides composition (with slender band gap values)⁴⁶ of the catalyst electrodeposited by the RoDSE technique in this work, allows its classification as quantum dots.^{17,18} The electron diffraction pattern confirms iron-oxide based species (SI Figure S4), which confirm that the oxidation process was accelerated during the preparation sample for microscopic analysis. These results confirm that the catalyst synthesized consists of iron-based quantum dots onto Vulcan XC-72R. This Fe–C configuration will determine a synergetic contribution during

the ORR kinetic. TEM studies showed nanoparticle size, shape, distribution, and partial structure information.

X-ray Diffraction (XRD) Measurements. To obtain information regarding iron nanoparticle surface and crystal structure, X-ray diffraction (XRD) measurements were done on the iron-based catalyst synthesized by the RoDSE Technique. As are shown in SI Figure S5, XRD analyses evidence iron-based nanostructures on the carbon support. The broadness and ill-definition of the diffractogram peaks are characteristic of tiny nanostructures.⁴⁷ The average particle size was not calculated using Scherrer's equation due to the heterogeneous composition of the catalyst, broadness of peaks due to nanoscale nature, the Fe/C-peak-ratios, and iron oxidation process, will be affecting the size determination by

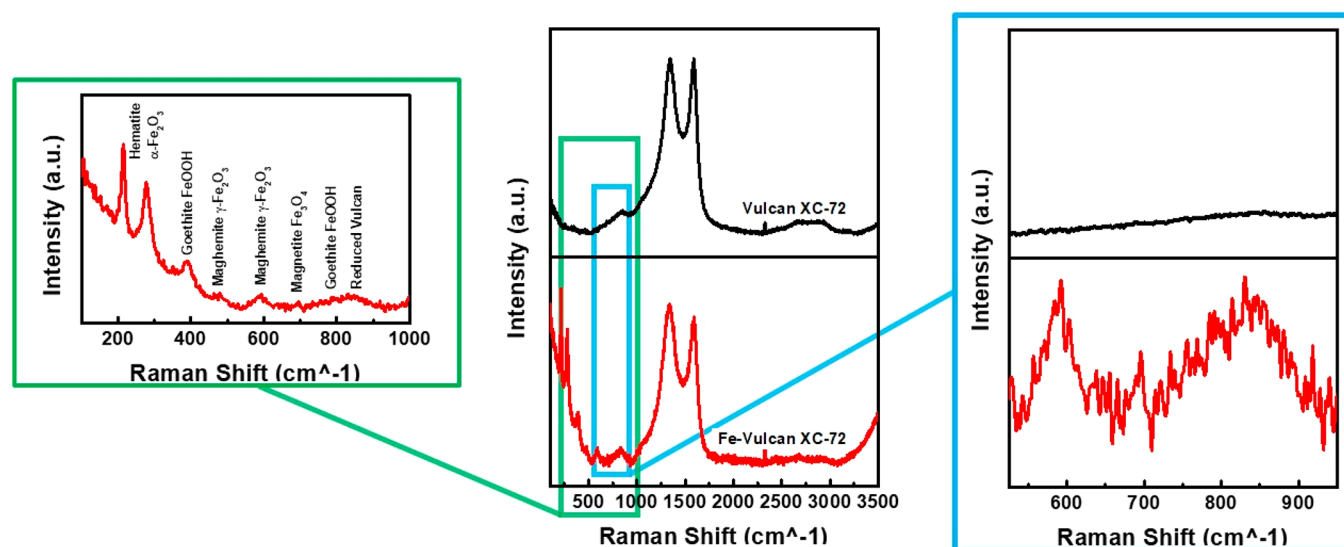


Figure 6. Raman spectra of the Vulcan XC-72R before and after the iron electrodeposition (Fe/Vulcan) by the RoDSE technique. Enlarged views of the characteristic regions of iron compounds are shown in both sides of the main Raman figure.

XRD analysis. The diffractogram shows a typical α -Fe diffraction pattern with a peak located at 2θ about to 46.1° , corresponding to the facet (110) (JCPDS card no. 06–0696). The other iron facets, (200) and (211), are not seen due to low intensity in comparison with the carbonaceous matrix response. Two intense and broad peaks of carbon materials appear at the characteristic 2θ equal to 24.4° and 43.3° , corresponding to the diffraction planes (002) and (101), respectively (JCPDS card no. 41–1487). The indexed reflection (002) line is a result of the interlayer scattering of Vulcan XC-72R, whereas the intralayer scattering develops the (101) line. It is noted that the peak intensity of carbon faces significantly decreased and modified their shapes after the Fe was electrodeposited. This indicated that the iron nanostructures have been deposited on the Vulcan XC-72R. Oxidation of iron is evidenced by the presence of other peaks that could be associated with the pattern of magnetite (Fe_3O_4), maghemite ($\gamma\text{-Fe}_2\text{O}_3$), hematite ($\alpha\text{-Fe}_2\text{O}_3$), goethite ($\alpha\text{-FeOOH}$), or lepidocrocite ($\gamma\text{-FeOOH}$). Due to its high surface area and greater availability of surface reactive sites, the iron QDs obtained by the RoDSE technique are corrode faster than bulk metallic iron.^{48,49} The Iron QDs electrodeposited in this work, is constituted of different shells of oxides. The structure will be defined as a gradient of oxide layers, moving from the metallic iron nanoparticles in the core, followed by an inner layer of magnetite and outer layer of maghemite and ferrihydrite. Our system could be demarcated as a combination of corrosive transformation products as follows: Fe^0 to $\text{Fe}^{2+/3+}$ to Fe^{3+} , where the oxidation ratio gradient will be determined by the synthesis process, particle size, storage conditions, longevity, and sample manipulation during the characterization protocols. These insights are supported by previous reports, on which the geometry and size of nanoparticles allow fast oxidation through a cation diffusion mechanism in air-based environments during short periods of time and at room temperature.⁴⁹

If the 2 nm of radio that owns the Fe QDs synthesized by the RoDSE technique, are taken into consideration, the iron oxidation evolution, as a function of time, is an extremally fast process. Likewise, the initial oxidation process of the Fe QDs could be described as an initial attachment of oxygen onto the

surface of the Vulcan, forming a thin layer of oxide on the metal surface. The electron, generated in the redox process, tunnels through the oxygen functionalities, and produces an electrical field between the Fe-core and the external oxidized shell. Finally, the reminder iron in the core will subsequently drive outward diffusion of the ionized iron, generation complex matrix of iron-, and oxygen-based compounds.⁴⁹

Raman Spectroscopy. To understand the particle-substrate structures on the catalyst synthesized, the nature of the iron and carbon species were resolved by Raman spectroscopy. Figure 6 shows the Raman spectra of the Vulcan XC-72R before and after the iron electrodeposition. A subtle-peak at $1050\text{--}1100\text{ cm}^{-1}$ is shown for the Vulcan XC-72R carbon support. This peak can be attributed to the an sp^3 rich phase in the carbon configuration.⁵⁰ The width and intensity generated in this region decrease after iron electrodeposition on the surface.

The main contributing crystalline forms of carbon, graphitic and diamond, have been well studied. The diamond has a face-centered cubic crystallographic structure and is characteristic of the C–C single bonds between sp^3 hybridized carbon atoms with a band located at 1350 cm^{-1} D-band. The G-band corresponding to the E_{2g} symmetry is localized around 1580 cm^{-1} . The amorphous sp^2 phase of carbon should be convoluted between the D and G bands while the sp^3 -rich phase appears centered at 1180 cm^{-1} .¹⁵ D and G bands from graphitic E_{2g} modes were identified about 1350 and 1580 cm^{-1} , respectively, for both the carbon support material and the Fe QDs electrodeposited by the RoDSE technique. Raman spectrum. A small protuberance that broad the peak was noticed for Vulcan XC-72R at around $1600\text{--}1650\text{ cm}^{-1}$.^{15,20}

The degree of graphitization of these carbonaceous materials, $I^{\text{D}}/I^{\text{G}}$ ratio, is used to quantify the number of defects in the iron- and carbon-based materials before and after of the electrodeposition process by the RoDSE technique. Figure 6 shows the spectra for the carbon substrate before modification and for the iron–carbon sample. The modified sample shows an increase in the D/G ratio, in effect showing a lower area for the graphitic and sp^2 -rich peak. The higher $I^{\text{D}}/I^{\text{G}}$, in comparison with the value for pristine Vulcan, can be

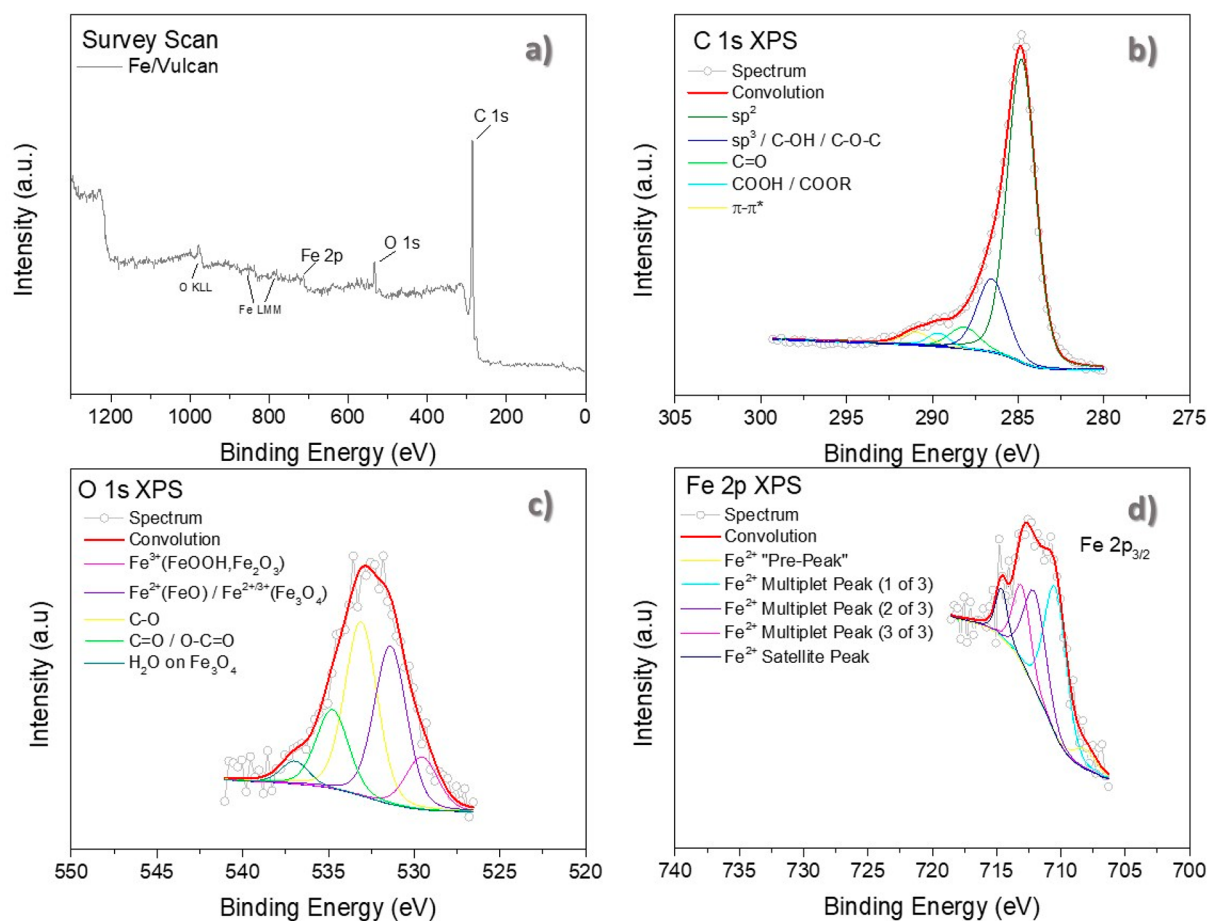


Figure 7. X-ray photoelectron spectroscopy survey scan (a), and the Voigt deconvolution analysis of the C 1s (b), O 1s (c), and Fe 2p_{3/2} (d) binding energy regions for the iron-based QDs onto Vulcan XC-72R electrodeposited by the RoDSE technique.

attributed to the iron nanostructures electrodeposited onto Vulcan XC-72R surface.

A broad and small peak about 850 cm⁻¹ corresponds to the hydrogen-free carbon structures. Although this peak increase after the iron deposition process, indicating that Vulcan is partially reduced during the synthesis, this peak could be a contribution of the iron oxides like hematite.⁵¹ Hematite is evidenced through the presence of the peaks at 212 and 280 cm⁻¹. The peak at 398 cm⁻¹ corresponds to goethite. The peaks at 477 and 590 cm⁻¹ are characteristics of maghemite, and the peak at 698 cm⁻¹ is magnetite,⁵² agreeing with the gradient of oxidized iron species.

Surface Analysis by X-ray Photoelectron Spectroscopy (XPS). X-ray photoelectron spectroscopy (XPS) was used to determine the chemical composition of iron-based catalysts surface. Figure 7 shows the XPS spectra of iron-based QDs electrodeposited on Vulcan XC-72R by RoDSE Technique. The XPS of Fe 2p, C 1s, and O 1s binding energy region, obtained for the synthesized samples, were deconvoluted and analyzed using Multipack Physical Electronics curve-fitting program (see Figure 7). After a Shirley background subtraction, the C 1s, O 1s, and Fe 2p_{3/2} peaks were deconvoluted via Voigt profile analysis,⁵³ into Gaussian–Lorentzian components, with similar FWHM. The χ^2 values were lower than six units for all analyses. C 1s peak at 284.5 eV was used as a reference to correct the binding energies scale. SI Table S2 shows the binding energies of carbon functionalities from the literature.¹⁵

Figure 7 shows the C 1s binding energy spectrum with its respective peak contribution analysis of Fe/Vulcan catalyst.^{15,20} The deconvoluted peaks are related to surface functional groups as follow: graphitic sp² carbon (284.8 eV), C–OH/C–O–C sp³ (286.5 eV), carbonyl species (288.1 eV), COOH/COOR groups (289.6 eV), and p-p* transitions (290.9 eV), see Table 1. The main C 1s deconvoluted constituent, which correspond to sp² carbon hybridization state, appear at approximately 284.8 eV. The percentage ratio for this peak is above 71%, being the highest carbon component, and indicating that the nonfunctionalized carbon state dominates the support matrix configuration. The collection of peaks with binding energies between 286.1 and 288.6 eV could be attributed to carbon atoms bonded to oxygen in molecular species such as hydroxyl, carboxyl, or carboxylic groups. The oxygen-based functional groups on the carbon surface add hydrophilic characteristics to the carbon support and make its structure more accessible to the aqueous electrolyte and the iron precursor species. Furthermore, oxygen-based sites can act as anchoring-nucleation sites. The oxygen-based functional groups on the carbon surface represent anchoring groups for the iron nanostructures formed by the RoDSE technique. The surface oxygen functionalities that reached over 26% can generate partial-oxidation-sites for the Fe-QDs at the Vulcan support.

The O 1s deconvolution is shown in Figure 7, where the O 1s binding energy peak assignments⁵⁴ were 529.6, 531.4, 533.1, 534.8, and 537.0 eV, associated with Fe³⁺ (FeOOH/Fe₂O₃),

Table 1. XPS Oxidation State Contribution (%) of the C 1s, O 1s, and Fe 2p_{3/2} Binding Energy Components for the Fe/Vulcan XC-72R Catalyst Synthesized by the RoDSE Technique

binding energy region	interaction assignments	binding energy (eV)	ratio contribution (%)
C 1s	graphitic sp ²	284.8	71.16
	C-OH/C-O-C sp ³	286.5	17.95
	carbonyl species	288.1	5.37
	COOH/COOR groups	289.6	2.49
	π-π*	290.9	3.03
O 1s	Fe ³⁺ (FeOOH/Fe ₂ O ₃)	529.6	10.88
	Fe ²⁺ (FeO) and Fe ^{2+/3+} (Fe ₃ O ₄)	531.4	32.74
	C-O	533.1	36.05
	C=O/O-C=O	534.8	16.31
	H ₂ O on iron oxide	537.0	4.03
Fe 2p _{3/2}	Fe ²⁺ “pre-peak”	708.1	5.58
	Fe ²⁺ multiplet peak (1 of 3)	710.4	41.74
	Fe ²⁺ multiplet peak (2 of 3)	712.0	27.47
	Fe ²⁺ multiplet peak (3 of 3)	713.0	17.18
	Fe ²⁺ satellite peak	714.6	8.03

Fe²⁺(FeO) and Fe^{2+/3+}(Fe₃O₄), C-O, C=O/O-C=O, and water molecules on the iron oxide surface,⁵⁵ respectively. Around 44% of surface oxygen XPS binding energy signal came from the iron oxide species (see Table 1).⁵⁴

The Fe 2p XPS spectrum in Figure 7d exhibited a minimal peak signal, closely to the noise level (see SI Figure S6). The contribution of each iron component is summarized in Table 1. Since iron presence was determined by CV, XRD, ICP-OES, and TEM; Fe 2p spectrum was fitted evaluating deconvoluted peaks of metallic, oxides, and oxyhydroxides iron species. The

abundance of Vulcan XC-72R support may block the 2p metallic iron and rusted species.^{15,20} The broadness of these Fe 2p peaks is due to the generation of electrostatic interactions, crystal field exchanges, and the spin-orbit coupling among the 2p core-holes and the unpaired 3d electrons of the photoionized iron (II/III).^{56,57} The small size of the iron nanostructures, their dispersion on the widespread carbonaceous matrix, and the unique interaction of iron atoms with X-ray are factors that determine the low sample signal collected in the Fe 2p region.

The peak assignments for the Fe 2p_{3/2} components are reported in the Table 1. The Fe 2p_{3/2} and Fe 2p_{1/2} binding energy peak assignments are 712.1 and 725.8 eV, respectively. Fe binding energies and the ΔE = 13.7 eV between the Fe 2p_{3/2} and Fe 2p_{1/2} peaks are characteristic values for iron compounds. The peak assignment for the transition metals and compounds with high-spin must consider multiplet contribution in their fitting processes. High-spin Fe(II) and Fe(III) species contain unpaired d electrons and consequently exhibit multiplet splitting structures.^{54,56,57} The deconvolution analysis of the Fe 2p region into their spin-orbit split multiplet components is overextended. Hence, it is considered only the 2p_{3/2} signal⁵⁴ to evaluate the Fe-C composite gained by the RoDSE technique.

Being that iron particles are in the nanometer scale, their oxidation state will reflect the bulk oxidation state reported.^{54,57} Even assuming that a mixed iron metal/oxides nanoparticle system is dispersed on Vulcan, metallic iron will be inside, covered by oxygen-based compounds forming a core/shell-like structures.⁵⁸ The resulting triplet fitting plots suggests the presence of oxygenated Fe(II) species. However, the Fe(III) quadruplets fitting is complicated due to the low signal in the Fe 2p region.⁵⁴ Therefore, ferric oxidation state should be present, as well, due to the fast oxidation activation by the nanosize dimensions.

3.4. X-ray Absorption near Edge Structure (XANES) and Extended X-ray Absorption Fine Structure (EXAFS). The Fe K absorption edge exhibits higher sensitivity to both

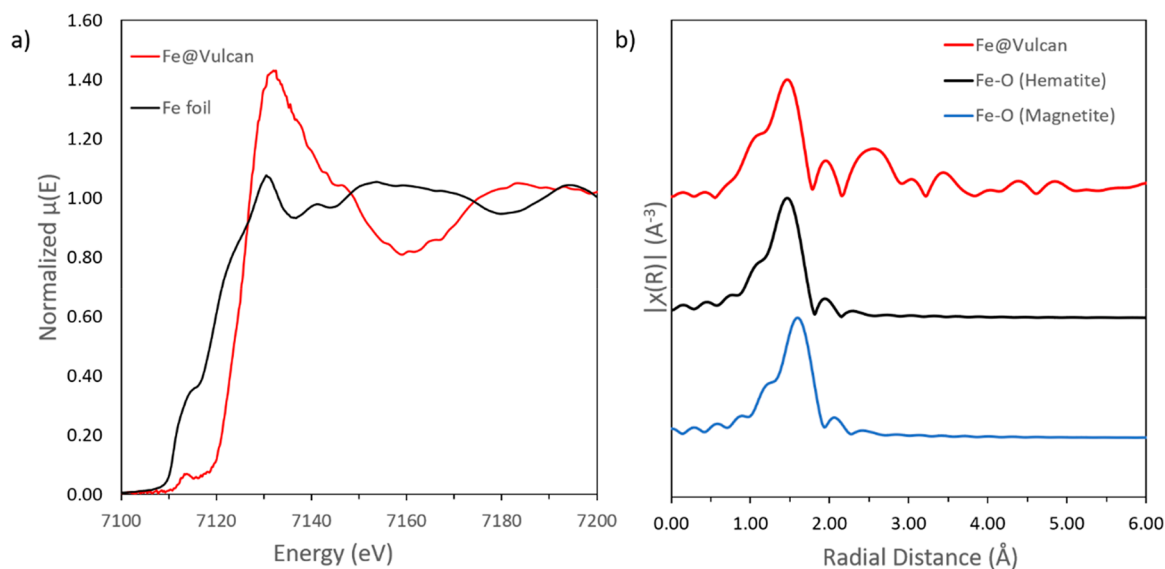


Figure 8. Comparison of X-ray absorption near edge structure (XANES) spectra (a) of Fe/Vulcan (red) and Fe metal foil (black). Comparison the Fourier transformed extended X-ray absorption fine structure (EXAFS) radial distribution signals taken at Fe K-edge for Fe/Vulcan (b), with k weight of 2, with the calculated single scattering paths contributions of hematite (black) and magnetite (blue).

oxidation state and differences in structure therefore making it an ideal candidate for XAS characterization analysis.²² Figure 8a shows the X-ray absorption near edge structure (XANES) spectra of electrodeposited iron on Vulcan and metallic iron for reference. The edge of the electrodeposited iron shows a clear energy shift toward higher energies relative to the iron metal foil. The intensity of the white line for Fe/Vulcan increases relative to that of the iron foil. Both observations suggest the presence oxidized iron. Fourier transformed extended X-ray absorption fine structure (EXAFS) signals taken at Fe K-edge for Fe/Vulcan is shown in Figure 8b. The strongest scattering contribution in the first coordination shell is observed at 1.44 Å, which is explained by the single scattering path of a Fe–O bond in the hematite (Fe₂O₃) crystal structure.⁵⁸ However, the apparent asymmetry of the peak in Fe/Vulcan, and the nature of iron oxides as they been exposed to air and humidity,⁴⁸ suggest a contribution of an Fe–O bond in magnetite (Fe₃O₄), as well. Overall, these findings correlate with the energy shift observed in the XANES spectra thus confirming that iron is in a higher oxidation state. SI Figure S7 shows XAFS data at the Fe edge for Fe/Vulcan catalyst and the Fe foil. Furthermore, it suggests that a mixture of hematite and magnetite is present. These results confirm the mixture of iron compounds reported above by XRD, TEM, Raman, and XPS.

3.5. Electrochemical Oxygen Reduction Reaction (ORR) kinetics by the Koutechy-Levich (K-L) analysis.

Hydrodynamic linear voltammetry trials were done to study the oxygen reduction reaction (ORR). The iron-based catalyst synthesized via the RoDSE method was tested in relation to its ORR catalytic activity in an O₂-saturated 0.1 M KOH solution, using a triple-compartment cell system, as is detailed in the experimental setup. Rotation speeds between 400 and 2400 rpm were employed to complete a steady-state polarization analysis of the Fe/Vulcan and the Vulcan XC-72R support (see SI Figure S8). The scan rate used was 10 mV/s, as typically expected in a steady-state polarization curve, the current density rises as the rotation speed is increased, that is, a proportional correlation between the rotation speed and the current density generated is revealed in the plots shown in SI Figure S8. Even though the last product is an oxide's mixture, all the QDs structures are efficiently controlled and electrochemically reduced to iron Fe⁰, as needed, by a tuning-treatment before runs any catalytic experiment, see SI Figure S9. Figure S9 shows that the iron reduction peak disappears after the first scanning process, indicating that iron species on the surface reduces to Fe⁰.

A Koutechy-Levich (K-L) analysis²¹ of the RDE data was done to evaluate the ORR kinetics and the transferred electron number (*n*-value), since the ORR redox process mechanism is related to the *n*-value. The K-L analysis was done by using eq 1:

$$\frac{1}{j} = \frac{1}{j_k} + \frac{1}{j_d} = \frac{1}{nFkC^0} + \frac{1}{0.62nFD_{O_2}^{2/3}\nu^{-1/6}C^0\omega^{1/2}} \quad (1)$$

where *j* is the measured current density at a given potential, *j_k* and *j_d* are the kinetic and diffusion limited current densities, *k* is the rate constant for O₂ reduction, *n* is the number of electrons involved in the oxygen reduction reaction, *F* is the Faraday constant (96485 C mol⁻¹), *ω* is the rotation rate (rad s⁻¹), *C*⁰ is the saturation concentration of O₂ in 0.1 M KOH at

1 atm O₂ pressure, *D_O* is the O₂ diffusion coefficient and *ν* is the solution kinematic viscosity.

As is shown in SI Table S3, the electron transfer number of Fe/Vulcan catalyst in 0.1 M KOH solution was calculated from the K–L plots to be 2.6, suggesting Fe/Vulcan catalyst favored a two-electron pathway oxygen reduction process. Whereas the calculation from the K–L plots of the Vulcan XC-72R revealed an electron transfer number of 1.6 in alkaline media. The Fe-based catalyst shows a higher limited diffusion current in comparison with Vulcan. A high electrocatalytic activity of Fe/Vulcan toward peroxide formation by electrochemical O₂ conversion in alkaline medium was observed.

An increment in the global activity is observed as an increase in the diffusion-limited current density (*j_D*). The half-wave potential (*E*_{1/2}) were 0.467, 0.573, and 0.785 V vs RHE for the Fe/Vulcan, Vulcan XC-72R, and Pt(20%)/C, respectively. Likewise, the onset potentials (*E*_{onset}) were 0.566, 0.642, and 0.876 V vs RHE for Fe/Vulcan, Vulcan XC-72R, and Pt(20%)/C, respectively. SI Figure S8 exhibited a linear relationship between the limiting current density and the rotation speed rate for each material analyzed. Modifying Vulcan with Fe increased the diffusion limited current density (*j_D*) and shifted the ORR half wave potential to more negative potential values. In comparison to Vulcan, the onset potential is slightly modified along with an overall activity increment observed as a current increase. The Fe/Vulcan catalytic activity, in terms of the *n_e* transfer capacity and the current density, displays enhanced performance in ORR to peroxide efficiency via two-electron pathway. The introduction of iron QDs onto conductive carbonaceous substrates significantly influences the catalytic activity of the oxygen reduction kinetic toward hydrogen peroxide production.

Vulcan suffers modifications in its surface after the electrodeposition process by the RoDSE technique.²⁰ Although the Fe/Vulcan *E*_{onset} and *E*_{1/2} parameters slightly decrease, as compared with Vulcan, iron helps to reach the *j_D* that is necessary to produce an effective ORR. The iron QDs and structural modifications of Vulcan after the RoDSE process may tailor the electronic structure of the iron–carbon combination. This further indicates that the ORR is strongly dependent on the nature of the active sites present on the surface. Iron improves the activity for the oxygen reduction kinetics, but just the necessary to produce H₂O₂, that is, via two electrons. It is seen that peroxide generation could be controlled as a function of the applied potential. A more in-depth analysis was done via RRDE and in situ production experiments, as is explained below.

3.6. Rotating Ring-Disk Electrode (RRDE) for H₂O₂ Analysis.

The linear sweep voltammetry for ORR kinetics with the Rotating Ring Disk Electrode (RRDE) technique of Fe/Vulcan in O₂-saturated 0.1 M KOH is shown in Figure 9. A potential window between –400 and 500 mV vs RHE was used for the RDE while the Pt ring was maintained at 1.2 V vs RHE. This plot shows the results of steady-state RRDE experiments at a rotation speed of 1600 rpm. The cathodic peak wave (blue line) shows an increase in the current as a function of the potential sweep, which confirms diffusion and controlled ORR at the catalyst surface. These experiments showed reproducibility after three different inked-electrode tests. The cathodic current at potentials between –400 and 600 mV is attributed to the O₂ reduction. The *E*_{onset} potential of the ORR is observed near 570 mV, with diffusion limited behavior being achieved between –400 and 150 mV vs RHE.

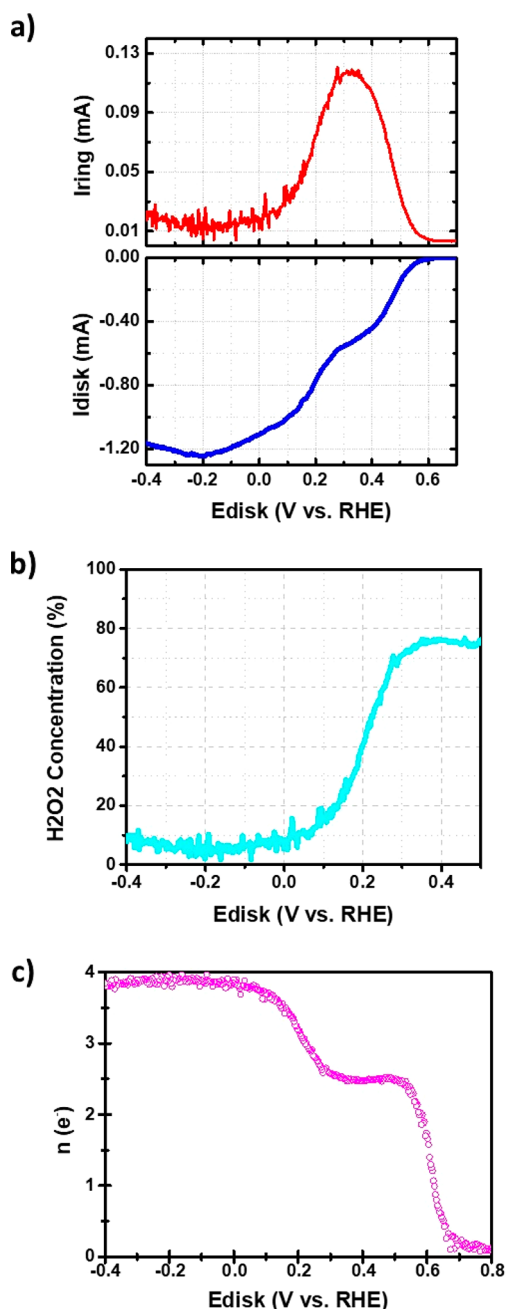


Figure 9. Data collected during the hydrodynamic RRDE study of Fe/Vulcan for the ORR as a function of potential vs RHE. (a) Plot of the disk current, I_{disk} (dark blue line) and ring current, I_{ring} (red line). (b) Concentration of hydrogen peroxide (% H_2O_2 ; light blue line) vs E_{disk} vs NHE. (c) Number of electrons (n) involved in the oxygen reduction reaction. The RRDE analysis was completed by testing Fe/Vulcan ink on glassy carbon disk and Pt ring in KOH 0.1 M. The Fe/Vulcan/GC disk electrode potential was swept at a scan rate of 10 mV/s, the Pt ring potential was fixed at 1.20 V vs RHE, and the RRDE rotation speed was 1600 rpm.

Fe/Vulcan catalyst shows a diminution in the diffusion limited current as the potential becomes less positive in the diffusion limited region between -400 and -200 mV vs RHE. This suggests a decrease in the n -value, related to the mechanism of oxidation in this region (based on the K-L analysis).

The ring-current, associated with the hydrogen peroxide formation-degradation process, is plotted (top-red line) with

data collected simultaneously during the hydrodynamic RRDE study. The H_2O_2 selectivity (% H_2O_2) and the electron transfer number (n) were calculated as follow:⁴

$$\% \text{H}_2\text{O}_2 = 200 \left(\frac{I_{\text{ring}}/N}{I_{\text{disk}} + I_{\text{ring}}/N} \right) \quad (2)$$

$$n = \left(\frac{4I_{\text{disk}}}{I_{\text{disk}} + \frac{I_{\text{ring}}}{N}} \right) \quad (3)$$

Where I_{ring} is the ring current, I_{disk} is the disk current, and N is the collection efficiency. As shown in Figure 9a, the highest detectable formation rates of stable peroxide were observed in 0.1 M KOH electrolyte solution at low potentials. The number of electrons (n) and H_2O_2 concentration were calculated using eq 2 and eq 3. Figure 9b,c evidenced a 75% of H_2O_2 production and a n value of 2.5, in KOH 0.1 M at a potential window between 350 and 450 mV. Based on the total peroxide concentration and the current production, it could be inferred that Fe/Vulcan promotes the reactions $\text{O}_2 + 2\text{H}^+ + 2\text{e}^- \rightarrow \text{H}_2\text{O}_2$ and $\text{O}_2 + 4\text{H}^+ + 4\text{e}^- \rightarrow 2\text{H}_2\text{O}$, simultaneously, contesting themselves as the applied potential is swept.

The RRDE experiments were focused on determining the rate of hydrogen peroxide formation and its electrochemical stability over the reaction time. A fixed voltage of 1.2 V was applied in the Pt-ring during the ORR hydrodynamic catalytic analysis. A differentiating current slope change is observed, that are maintained during specific ranges of potential. This distinctive stages, previously reported by Hasche et al.,⁵⁹ are associated with different stages in the ORR kinetics. A detailed evaluation of the ring-current curve shown in Figure 9a, allows a comprehensive lifetime understanding of the hydrogen peroxide in the potential window swept. Stage I, at a potential above 600 mV vs RHE, no peroxide formation was observed. Stage II, in the potential range between 350 and 600 mV vs RHE, the current increase indicates the formation of peroxide is promoted. In stage III, higher current is observed and is more stable between 250 and 350 mV. Stage IV, between 300 to 0 mV, represents a rate of H_2O_2 consumption where peroxide is used on the ring is higher than the formation on the disk. Finally, the peroxide formation is low but is stable in stage V in the potential window between 0 and -400 mV. Notwithstanding hydrogen peroxide formation is weak in this last potential range, the stability of the production in a broad potential-window is remarkable (see Figure 9b). At more negative potentials, the current density is higher, but the current efficiency for hydrogen peroxide formation is lower. Figure 9c shows that at potentials more negative than 150 mV, the number of electrons (n) involved is about 4. Also, this decrease in current efficiency is attributed to the cathodic reduction of H_2O_2 to hydroxide ions. Although the onset potential of this material is shifted toward more negative potentials versus the commercial Pt-based catalyst, Fe/Vulcan looks as a potential candidate to study its 4-electron transfer of this catalyst for energetic applications. For this, it will be necessary to redesign the catalyst to shift the potential window toward more positive values, reducing the ORR overpotential with respect to platinumized catalysts. As shown in Figure 9a, the highest detectable formation rates of stable peroxide were observed in 0.1 M KOH at the potential window between 300 and 500 mV.

The RRDE analysis reflects that the Fe/Vulcan catalyst, electrodeposited by the RoDSE technique, produces a high fraction of hydrogen peroxide intermediate at potentials higher than 0.3 V, a region characteristic of the cathode operation in a fuel cell.⁶⁰ Likewise, the reduction of the carbon structure, intrinsically generated on the carbon matrix material during the electrodeposition process, will avoid electrolyte flooding in the cathode. The RoDSE technique produces a Fe–C catalyst that, after loading it on gas diffusion layer electrodes, will provide of three-phase contact points for oxygen, electrolyte, and catalyst.⁷ This makes this iron- and carbon-based material suitable for in situ peroxide production for space applications.

3.7. In Situ Electrochemical Hydrogen Peroxide Generation for Space Applications. Based on the RRDE results, Fe/Vulcan catalyst was chosen to be tested in the operating conditions resources for space applications, specifically for producing surface cleaning/sanitizing solutions using on-board life-support supplies. Secure-cleaned environments represent one of the several technological challenges faced by human closed-loop living systems during space missions.^{1,8}

The experiments were done in an in situ prototype generation unit (PGU) developed by Faraday Technology Inc. and the University of Puerto Rico.¹ A single-pass catholyte process flow stream was utilized to determine the best variable configuration for future experiments under microgravity conditions. The PGU was done consequently to the compatibility of the drinking water resources available in the International Space Station (ISS): 2–3 mS/cm of conductivity, a pH window between 5.5 and 6.7, and total organic carbon (TOC) concentration range between 0.18 and 2.5m/L.⁸ The electrochemical reactor system schematic, with inputs and outputs, is shown in SI Figure S10.

The cathode consists of a catalyzed gas diffusion electrode pressed fed with a gas stream containing oxygen at a target back pressure. The reaction taking place at the cathode is $O_2 + H_2O + 2e^- \rightarrow HO_2^- + OH^-$. This reaction only occurs at the catalyzed gas diffusion electrodes surface in the presence of oxygen and water. If the gas diffusion electrode does not sufficiently create a gas water barrier or consists of the wrong catalytic materials the reaction could proceed fully to water. The central chamber for the peroxide generator consists of an ion exchange media (beads) in between the GDE and cation electrolyte membrane (CEM) that enables the transfer of ions across the catholyte stream. Finally, the anode chamber consists of a mixed metal oxide pressed against the cation electrolyte membrane within a vented compartment. The reaction taking place at the anode is $H_2O \rightarrow 1/2 O_2 + 2H^+ + 2e^-$. The water necessary for the anode reaction, and to allow ion transfer across the cation electrolyte membrane, is provided from the catholyte. Giving a total system reaction of $1/2 O_2 + H_2O \rightarrow H_2O_2$.

The PGU results are shown in Figure 10. In this case, ink dispersions of Fe/Vulcan were painted onto new GDEs. Differential polarization trials were done at the processing conditions explained in the Experimental section. Peroxide generation performance was determined at 4, 6, 8, and 10 V. Potentials of 12 and 14 V were aimed to be tested, but the output currents were highly unstable due to bubbles formation inside the chamber.

The single-pass polarization trial results, conducted using GDE-MPL and Fe/Vulcan coated GDE, are shown in Figure 10. Meaningful currents were observed as concomitant with an increase in voltages for the iron-based catalyst, with the highest

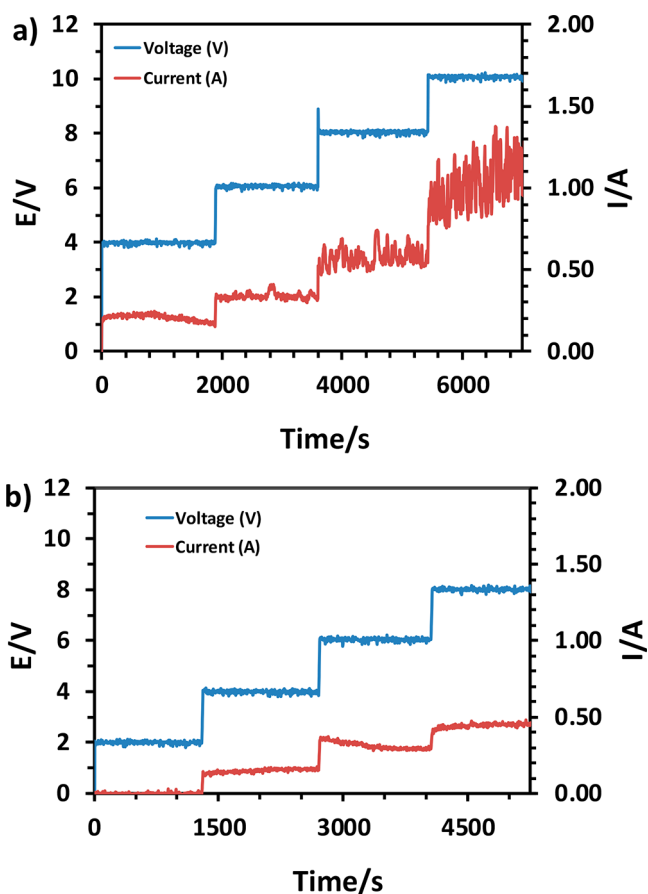


Figure 10. Polarization curves for the *in-situ* hydrogen peroxide generation on the Fe/Vulcan (a) and the GDE (b). Polarization curves of Fe/Vulcan and the GDE-MPL were done in RO water at different potentials.

current being at 6 V. The comparison of catalyst trial results is shown in Table 2.

Table 2. *In-situ* H_2O_2 Generation and Output Current Produced by the GDE-Fe/Vulcan and GDE-MPL Catalysts at an Applied Voltage of 4, 6, and 8 V

E (V)	Fe/Vulcan		GDE-MPL	
	H_2O_2 concentration (w/w%)	I (A)	H_2O_2 concentration (w/w%)	I (A)
4	0.024	0.17	0.006	0.16
6	0.056	0.35	0.030	0.28
8	0.032	0.55	0.050	0.44

SI Figure S11 shows a comparative plot of hydrogen peroxide production and the output current by the Fe/Vulcan at different voltages, utilizing oxygen and RO water as electrolyte. Fe/Vulcan and GDE-MPL can generate 0.055 and 0.030 w/w% H_2O_2 , respectively, at 6 V. Whereas, the system output currents were 0.35 A for Fe/Vulcan and 0.28 A for GDE-MPL. These results suggested that Fe/Vulcan showed high selectivity toward a two-electron pathway reduction process at 6 V. It represents a promising result, having in consideration that the RO water low conductivity (2–3 mS/cm), used in this system, is electrochemically unfavorable.

Additionally, the output current of the GDE-MPL at 6 V significantly decreases as a function of time. Its exponential

decay behavior (see SI Figure S12) indicates a possible decomposition of the carbon in the GDE-MPL surface, and a consequent penetration of water in the cathode. After opening the PGU, we observed water presence in the cathodic side. In fact, the GDE-MPL trial current decreased exponentially in seconds from (3120 s, 0.315 A) to (3840 s, 0.281amps), with (time, current) as (x,y) coordinates. On the other hand, the RoDSE electrodeposited Fe/Vulcan catalyst remained unchanged in the same time window.

Consequently, the efficiency increased by 87% for hydrogen peroxide production in RO water by using Fe/Vulcan catalyst. For this, 0.056 w/w% (560 ppm) of hydrogen peroxide concentration obtained via single-pass for the Fe/Vulcan composite are compared with the 0.030 w/w% (330 ppm) for the GDE-MPL. Equally promising, an increment of 25% in current in RO water is earned when the 0.35 A output current for Fe/Vulcan is compared with the 0.28 A generated by the GDE-MPL trial.

The current results indicate that Fe/Vulcan outperform the commercial GDE-MPL at the studied potentials. Fe/Vulcan is a promising catalyst to use in the PGU at low potentials (4 and 6 V) to develop in future experiments. Peroxide production in lower voltages increases the catalyst lifetime, reduces the probability of water-splitting process, and decreases bubbles formation inside of the reactor. In future studies, a recycle loop orientation to increase the hydrogen peroxide concentration will be done. Moreover, the catalyst stability in the PGU will be studied under extended operation periods, as well as, under microgravity conditions.

4. CONCLUSIONS

An electrochemical method that reduces a Fe^{3+} precursor, forming homogeneously distributed iron-based quantum dots onto a solid carbonaceous matrix has been demonstrated. The RDE, RRDE, and PGU experiments revealed a high activity for the ORR via two-electron pathway. The FeQDs/Vulcan electrodeposited by the RoDSE technique is a promising catalyst to be used in PGU at low potentials of 4 and 6 V. The in situ obtention of hydrogen peroxide, under compatibility conditions of the drinking water resources available in the ISS, triggers up the Fe/C catalyst for the ORR in space missions. Future experiments will be done using a recycle loop orientation to increase the hydrogen peroxide concentration, as well as tests under microgravity conditions.

Transmission electron microscopy analysis reveals the well-dispersed Fe quantum dots with a particle size of 4 nm, with a narrow size-distribution between 2 and 6 nm. Carbon support played an important role by offering anchoring-nucleation sites, avoiding nanoparticle agglomeration, and providing a conductive framework for enhanced ORR. The structural and chemical-physical characterization, through ICP, TEM, STEM, HAADF-STEM, XRD, Raman spectroscopy, XANES and EXAFs, exposes that the Fe quantum dots system is demarcated as a combination of corrosion-transformation products as follow: Fe^0 to $\text{Fe}^{2+/3+}$ to Fe^{3+} . The oxidation ratio gradient can be controlled by the synthesis process, particle size, storage conditions, longevity, and sample manipulation during the characterization protocols. Even though, under atmospheric conditions, the iron-based quantum dots remain as an oxidized gradient configuration, their tunability was shown by the applied potential. Before each ORR kinetics experiment, the iron-based QDs were reduced to Fe^0 . Likewise, the abundant three-phase contact points for the ORR are

distinguishing properties of the Fe/Vulcan catalyst synthesized in this work.

Terrestrial and space abundance of iron and carbon, its low toxicity, and high stability suit with the parameters established by the US DoE Strategic Plan. Our approach is to switch the nanocarbon source and metal-carbon configurations, to control the two-electrons route in the ORR kinetics for fuel cells in space technologies. This consolidates our present work as a large-scale production process of highly active Fe nanoparticles for in situ H_2O_2 generation.

Likewise, the origin of the current transients, generated during the RoDSE technique, are associated with the Fe/Vulcan and $\text{H}_2\text{O}/\text{H}^+$ couple interactions through electro-catalytic amplification. The enhanced current transients open the possibility to design a fluidized bed reactor-like, to study the electrochemical amplification reactions where the electro-catalyst is used as a label to obtain higher yields. Accurately, large-scale production of treasured gases for human space missions via electrochemical amplification of the HER and OER, to produce large quantities of gases such as H_2 and O_2 , represents a fascinating research field.

■ ASSOCIATED CONTENT

Supporting Information

The Supporting Information is available free of charge at <https://pubs.acs.org/doi/10.1021/acsami.1c05649>.

Cyclic voltammetry profiles, induced coupled plasma-optical emission spectroscopy (ICP-OES) results, TEM electron diffraction patterns, X-ray diffraction (XRD) measurements, X-ray photoelectron spectroscopy (XPS) of Fe 2p binding energy region, XAFS, rotating-disk electrode polarization curves, hydrogen peroxide production and the output currents, and polarization curve for the in situ hydrogen peroxide generation on the GDE-MPL at 6 V (PDF)

■ AUTHOR INFORMATION

Corresponding Authors

Armando Peña-Duarte – Department of Physics, University of Puerto Rico, San Juan, Puerto Rico 00926, United States;

orcid.org/0000-0002-4286-5278;

Email: armando.pena@upr.edu

Carlos R. Cabrera – Department of Chemistry, University of Puerto Rico, San Juan, Puerto Rico 00926, United States;

orcid.org/0000-0002-3342-8666;

Email: carlos.cabrera2@upr.edu

Authors

Santosh H. Vijapur – Faraday Technology Inc., Englewood, Ohio 45315, United States; orcid.org/0000-0001-9033-9697

Timothy D. Hall – Faraday Technology Inc., Englewood, Ohio 45315, United States; orcid.org/0000-0002-4756-0828

Kathleen L. Hayes – Department of Chemistry and Biochemistry, University of Notre Dame, Notre Dame, Indiana 46556, United States; orcid.org/0000-0003-1217-0050

Eduardo Larios-Rodríguez – Departamento de Ingeniería Química y Metalurgia, Universidad de Sonora, Hermosillo, México 83000, United States; orcid.org/0000-0001-8392-6666

Joselyn Del Pilar-Albaladejo – Department of Chemistry, University of Puerto Rico, San Juan, Puerto Rico 00926, United States

Mitk'El B. Santiago – Department of Chemistry, Universidad Ana G. Méndez, San Juan, Puerto Rico 00926, United States

Stephen Snyder – Faraday Technology Inc., Englewood, Ohio 45315, United States

Jennings Taylor – Faraday Technology Inc., Englewood, Ohio 45315, United States; orcid.org/0000-0002-3410-0267

Complete contact information is available at: <https://pubs.acs.org/10.1021/acsami.1c05649>

Notes

The authors declare no competing financial interest.

ACKNOWLEDGMENTS

We express our gratitude of both NASA Fellowship from NASA Puerto Rico Space Grant Consortium No. NNX15AI11H at the UPR, and the NASA Phase II SBIR Contract NNX16CA43P through Faraday Technology Inc. This work was supported by the National Science Foundation NSF-PREM: Center for Interfacial Electrochemistry of Energy Materials (CiE2M) grant number DMR-1827622. The use of the Cornell Center for Materials Research Shared Facilities, which are supported through the NSF MRSEC grant number DMR-1719875, are greatly appreciated. Also, we express our gratitude for NSF REU PR-CLIMB Grant No. 1560278. This research used resources of beamline (BMM) 6-BM of the National Synchrotron Light Source II in Brookhaven National Laboratory; a U.S. Department of Energy (DOE) Office of Science User Facility operated for the DOE Office of Science by Brookhaven National Laboratory under Contract DE-SC0012704. The RoDSE setup schematic was done in collaboration with Dra. Myreisa Morales and Mr. Jeriel Dumeng. We also thank Mr. Jeriel Dumeng for his participation in the iron tuning-treatment for the RDE study for the ORR.

REFERENCES

- (1) Nelson, G. J.; Vijapur, S. H.; Hall, T. D.; Brown, B. R.; Peña-Duarte, A.; Cabrera, C. R. Electrochemistry for Space Life Support. *Electrochem. Soc. Interface* **2020**, *29* (1), 47–52.
- (2) Winter, M.; Brodd, R. J. What Are Batteries, Fuel Cells, and Supercapacitors? *Chem. Rev.* **2004**, *104* (10), 4245–4270.
- (3) Li, Y.; Zhang, H.; Wang, S.; Lin, Y.; Chen, Y.; Shi, Z.; Li, N.; Wang, W.; Guo, Z. Facile Low-Temperature Synthesis of Hematite Quantum Dots Anchored on a Three-Dimensional Ultra-Porous Graphene-Like Framework As Advanced Anode Materials for Asymmetric Supercapacitors. *J. Mater. Chem. A* **2016**, *4* (29), 11247–11255.
- (4) Sánchez-Sánchez, C. M.; Rodríguez-López, J.; Bard, A. J. Scanning Electrochemical Microscopy. 60. Quantitative Calibration of the SECM Substrate Generation/Tip Collection Mode and Its Use for the Study of the Oxygen Reduction Mechanism. *Anal. Chem.* **2008**, *80* (9), 3254–3260.
- (5) Yeager, E. Electrocatalysts for O₂ reduction. *Electrochim. Acta* **1984**, *29* (11), 1527–1537.
- (6) Carrette, L.; Friedrich, K. A.; Stimming, U. Fuel Cells - Fundamentals and Applications. *Fuel Cells* **2001**, *1* (1), 5–39.
- (7) Lu, Z.; Chen, G.; Siahrostami, S.; Chen, Z.; Liu, K.; Xie, J.; Liao, L.; Wu, T.; Lin, D.; Liu, Y.; Jaramillo, T. F.; Nørskov, J. K.; Cui, Y. High-efficiency Oxygen Reduction to Hydrogen Peroxide Catalysed by Oxidized Carbon Materials. *Nature Catal.* **2018**, *1* (2), 156–162.
- (8) Vijapur, S. H.; Hall, T. D.; Taylor, E.; Wang, D.; Snyder, S.; Skinn, B.; Peña-Duarte, A.; Cabrera, C. R.; Sweterlitsch, J. *In-Situ*

Resource Utilization for Electrochemical Generation of Hydrogen Peroxide for Disinfection. *ICES: International Conference on Environmental Systems* **2019**, *38*, 14.

(9) Rutala, W. A.; Weber, D. J.; Healthcare, T.; Hicpac, I. C. P. A. C. *Guideline for Disinfection and Sterilization in Healthcare Facilities*. United States Centers for Disease Control and Prevention, 2008; http://www.cdc.gov/hicpac/pdf/guidelines/Disinfection_Nov_2008.pdf (accessed September 2020).

(10) Xia, C.; Xia, Y.; Zhu, P.; Fan, L.; Wang, H. Direct Electrosynthesis of Pure Aqueous H₂O₂ Solutions up to 20% by Weight Using a Solid Electrolyte. *Science* **2019**, *366* (6462), 226.

(11) Caruana, D. J.; Holt, K. B. Astroelectrochemistry: the Role of Redox Reactions in Cosmic Dust Chemistry. *Phys. Chem. Chem. Phys.* **2010**, *12* (13), 3072–3079.

(12) Energy, U. D. o. US Department of Energy Strategic Plan, at: <https://www.energy.gov/downloads/us-department-energy-strategic-plan-0>. March 31, 2021.

(13) Shimizu, K.; Sepunaru, L.; Compton, R. G. Innovative Catalyst Design for the Oxygen Reduction Reaction for Fuel Cells. *Chem. Sci.* **2016**, *7* (5), 3364–3369.

(14) Singh, B. P.; Kumar, A.; Duarte, A. P.; Rojas, S. J.; Crespo-Medina, M.; Areizaga-Martinez, H. I.; Vega-Olivencia, C. A.; Tomar, M. S. Synthesis, Characterization, and Electrochemical Response of Iron Oxide Nanoparticles for Sensing Acetaminophen. *Mater. Res. Express* **2016**, *3* (10), 106105.

(15) Betancourt, L. E.; Ortiz-Rodríguez, Á. M.; Corchado-García, J.; Cabrera, C. R. RoDSE Synthesized Fine Tailored Au Nanoparticles from Au(X)⁺ (X = Cl⁻, Br⁻, and OH⁻) on Unsupported Vulcan XC-72R for Ethanol Oxidation Reaction in Alkaline Media. *ACS Appl. Energy Mater.* **2019**, *2* (1), 287–297.

(16) Peña, A.; Puerta, J.; Guerrero, A.; Cañizales, E.; Brito, J. L. Catalytic Chemical Vapor Deposition Synthesis of Carbon Aerogels of High-Surface Area and Porosity. *J. Nanotechnol.* **2012**, *2012*, 5.

(17) Lindberg, V.; Hellsing, B. Metallic Quantum Dots. *J. Phys.: Condens. Matter* **2005**, *17* (13), S1075–S1094.

(18) Parak, W. J.; Manna, L.; Nann, T., *Fundamental Principles of Quantum Dots*. In *Nanotechnology. Vol. 1: Principles and Fundamentals*; Schmid, G., Ed.; WILEY-VCH Verlag GmbH & Co. KGaA: Weinheim, 2008.

(19) Santiago, D.; Rodríguez-Calero, G. G.; Rivera, H.; Tryk, D. A.; Scibioh, M. A.; Cabrera, C. R. Platinum Electrodeposition at High Surface Area Carbon Vulcan-XC-72R Material Using a Rotating Disk-Slurry Electrode Technique. *J. Electrochem. Soc.* **2010**, *157* (12), F189.

(20) Vélez, C. A.; Corchado-García, J.; Rojas-Pérez, A.; Serrano-Alejandro, E. J.; Santos-Homs, C.; Soto-Pérez, J. J.; Cabrera, C. R. Manufacture of Pd/Carbon Vulcan XC-72R Nanoflakes Catalysts for Ethanol Oxidation Reaction in Alkaline Media by RoDSE Method. *J. Electrochem. Soc.* **2017**, *164* (14), D1015–D1021.

(21) Koutetski, Y.; Levich, V. G. The Use of a Rotating Disc Electrode for Studying Kinetic and Catalytic Processes in Electrochemistry. *Dokl. Akad. Nauk SSSR.* **1957**, *117* (3), 441–444.

(22) Koningsberger, D. C.; Prins, R. *X-ray Absorption: Principles, Applications, Techniques of EXAFS, SEXAFS, and XANES*; New York: Wiley, 1988.

(23) Haupt, S.; Strehblow, H. H. Corrosion, Layer Formation, and Oxide Reduction of Passive Iron in Alkaline Solution: a Combined Electrochemical and Surface Analytical Study. *Langmuir* **1987**, *3* (6), 873–885.

(24) Grujicic, D.; Pestic, B. Iron Nucleation Mechanisms on Vitreous Carbon During Electrodeposition from Sulfate and Chloride Solutions. *Electrochim. Acta* **2005**, *50* (22), 4405–4418.

(25) Mallik, A.; Ray, B. C. Evolution of Principle and Practice of Electrodeposited Thin Film: A Review on Effect of Temperature and Sonication. *Int. J. Electrochem.* **2011**, *2011*, 568023.

(26) Grujicic, D.; Pestic, B. Electrodeposition of Copper: the Nucleation Mechanisms. *Electrochim. Acta* **2002**, *47* (18), 2901–2912.

- (27) Lee, J.; Kim, S.; Shinb, D. Electrodeposition of Iron in HNO₃ Solution Containing Iron Dissolved from Copper Slag. *J. Electrochem. Soc.* **2014**, *161* (14), D719–D724.
- (28) Zhang, H. Rotating Ring-Disk Electrode and Spectroelectrochemical Studies on the Oxidation of Iron in Alkaline Solutions. *J. Electrochem. Soc.* **1994**, *141* (3), 718.
- (29) Duschek, K.; Uhlemann, M.; Schlörb, H.; Nielsch, K.; Leistner, K. Electrochemical and In-Situ Magnetic Study of Iron/Iron-Oxide Films Oxidized and Reduced in KOH Solution for Magneto-Ionic Switching. *Electrochem. Commun.* **2016**, *72*, 153–156.
- (30) Beverskog, B.; Puigdomenech, I. Revised Pourbaix Diagrams for Iron at 25–300 °C. *Corros. Sci.* **1996**, *38* (12), 2121–2135.
- (31) Cornell, R. M.; Schwertmann, U. *The Iron Oxides: Structure, Properties, Reactions, Occurrences and Uses*, 2nd ed.; Wiley, 2003.
- (32) Shimizu, K.; Tschulik, K.; Compton, R. G. Exploring the Mineral-Water Interface: Reduction and Reaction Kinetics of Single Hematite (α -Fe₂O₃) Nanoparticles. *Chem. Sci.* **2016**, *7* (2), 1408–1414.
- (33) Zhou, X. S.; Mao, B. W.; Amatore, C.; Compton, R. G.; Marignier, J. L.; Mostafavi, M.; Nierengarten, J. F.; Maisonhaute, E. Transient Electrochemistry: Beyond Simply Temporal Resolution. *Chem. Commun.* **2016**, *52* (2), 251–263.
- (34) Kwon, S. J.; Bard, A. J. Analysis of Diffusion-Controlled Stochastic Events of Iridium Oxide Single Nanoparticle Collisions by Scanning Electrochemical Microscopy. *J. Am. Chem. Soc.* **2012**, *134* (16), 7102–7108.
- (35) Alligrant, T. M.; Anderson, M. J.; Dasari, R.; Stevenson, K. J.; Crooks, R. M. Single Nanoparticle Collisions at Microfluidic Microband Electrodes: The Effect of Electrode Material and Mass Transfer. *Langmuir* **2014**, *30* (44), 13462–13469.
- (36) Bard, A. J.; Zhou, H.; Kwon, S. J. Electrochemistry of Single Nanoparticles Via Electrocatalytic Amplification. *Isr. J. Chem.* **2010**, *50* (3), 267–276.
- (37) Zhang, H.; Sepunaru, L.; Sokolov, S. V.; Laborda, E.; Batchelor-McAuley, C.; Compton, R. G. Electrochemistry of Single Droplets of Inverse (Water-in-Oil) Emulsions. *Phys. Chem. Chem. Phys.* **2017**, *19* (24), 15662–15666.
- (38) Dick, J. E.; Bard, A. J. Toward the Digital Electrochemical Recognition of Cobalt, Iridium, Nickel, and Iron Ion Collisions by Catalytic Amplification. *J. Am. Chem. Soc.* **2016**, *138* (27), 8446–8452.
- (39) Jiang, J.; Huang, X.; Wang, L. Effect of Forced Convection on the Collision and Interaction Between Nanoparticles and Ultramicroelectrode. *J. Colloid Interface Sci.* **2016**, *467*, 158–164.
- (40) Kim, B.-K.; Boika, A.; Kim, J.; Dick, J. E.; Bard, A. J. Characterizing Emulsions by Observation of Single Droplet Collisions—Attoliter Electrochemical Reactors. *J. Am. Chem. Soc.* **2014**, *136* (13), 4849–4852.
- (41) Rees, N. V.; Banks, C. E.; Compton, R. G. Ultrafast Chronoamperometry of Acoustically Agitated Solid Particulate Suspensions: Nonfaradaic and Faradaic Processes at a Polycrystalline Gold Electrode. *J. Phys. Chem. B* **2004**, *108* (48), 18391–18394.
- (42) Klapper, H. S.; Zajec, B.; Heyn, A.; Legat, A. Elucidating Nucleation Stages of Transgranular Stress Corrosion Cracking in Austenitic Stainless Steel by In Situ Electrochemical and Optical Methods. *J. Electrochem. Soc.* **2019**, *166* (11), C3326–C3335.
- (43) Caballero-Briones, F.; Artés, J. M.; Díez-Pérez, I.; Gorostiza, P.; Sanz, F. Direct Observation of the Valence Band Edge by In-situ ECSTM-ECTS in p-Type Cu₂O Layers Prepared by Copper Anodization. *J. Phys. Chem. C* **2009**, *113* (3), 1028–1036.
- (44) Khaselev, O.; Sykes, J. M. In-situ Electrochemical Scanning Tunneling Microscopy Studies on the Oxidation of Iron in Alkaline Solution. *Electrochim. Acta* **1997**, *42* (15), 2333–2337.
- (45) Albu, C.; Van Damme, S.; Abodi, L. C.; Demeter, A. S.; Deconinck, J.; Topa, V. Influence of the Applied Potential and pH on the Steady-State Behavior of the Iron Oxide. *Electrochim. Acta* **2012**, *67*, 119–126.
- (46) Tamirat, A. G.; Rick, J.; Dubale, A. A.; Su, W.-N.; Hwang, B.-J. Using Hematite for Photoelectrochemical Water Splitting: a Review of Current Progress and Challenges. *Nanoscale Horiz.* **2016**, *1* (4), 243–267.
- (47) Miller, H. A.; Bellini, M.; Oberhauser, W.; Deng, X.; Chen, H.; He, Q.; Passaponti, M.; Innocenti, M.; Yang, R.; Sun, F.; Jiang, Z.; Vizza, F. Heat Treated Carbon Supported Iron(II)Phthalocyanine Oxygen Reduction Catalysts: Elucidation of the Structure-Activity Relationship Using X-ray Absorption Spectroscopy. *Phys. Chem. Chem. Phys.* **2016**, *18* (48), 33142–33151.
- (48) Pullin, H.; Springell, R.; Parry, S.; Scott, T. The Effect of Aqueous Corrosion on the Structure and Reactivity of Zero-Valent Iron Nanoparticles. *Chem. Eng. J.* **2017**, *308*, 568–577.
- (49) Wang, C. M.; Baer, D. R.; Thomas, L. E.; Amonette, J. E.; Antony, J.; Qiang, Y.; Duscher, G. Void Formation During Early Stages of Passivation: Initial Oxidation of Iron Nanoparticles at Room Temperature. *J. Appl. Phys.* **2005**, *98* (9), 094308.
- (50) Schwan, J.; Ulrich, S.; Batori, V.; Ehrhardt, H.; Silva, S. R. P. Raman Spectroscopy on Amorphous Carbon Films. *J. Appl. Phys.* **1996**, *80* (1), 440–447.
- (51) Hanesch, M. Raman Spectroscopy of Iron Oxides and (Oxy)Hydroxides at Low Laser Power and Possible Applications in Environmental Magnetic Studies. *Geophys. J. Int.* **2009**, *177* (3), 941–948.
- (52) Kwon, J. H.; Wilson, L. D.; Sammynaiken, R. Synthesis and Characterization of Magnetite and Activated Carbon Binary Composites. *Synth. Met.* **2014**, *197*, 8–17.
- (53) Jain, V.; Biesinger, M. C.; Linford, M. R. The Gaussian-Lorentzian Sum, Product, and Convolution (Voigt) Functions in the Context of Peak Fitting X-ray Photoelectron Spectroscopy (XPS) Narrow Scans. *Appl. Surf. Sci.* **2018**, *447*, 548–553.
- (54) Biesinger, M. C.; Payne, B. P.; Grosvenor, A. P.; Lau, L. W. M.; Gerson, A. R.; Smart, R. S. C. Resolving Surface Chemical States in XPS Analysis of First Row Transition Metals, Oxides and Hydroxides: Cr, Mn, Fe, Co and Ni. *Appl. Surf. Sci.* **2011**, *257* (7), 2717–2730.
- (55) Meier, M.; Hulva, J.; Jakub, Z.; Pavelec, J.; Setvin, M.; Bliem, R.; Schmid, M.; Diebold, U.; Franchini, C.; Parkinson, G. S. Water Agglomerates on Fe₃O₄ (001). *Proc. Natl. Acad. Sci. U. S. A.* **2018**, *115* (25), E5642.
- (56) Gupta, R. P.; Sen, S. K. Calculation of Multiplet Structure of Core *p*-Vacancy Levels. II. *Phys. Rev. B* **1975**, *12* (1), 15–19.
- (57) Grosvenor, A. P.; Kobe, B. A.; Biesinger, M. C.; McIntyre, N. S. Investigation of Multiplet Splitting of Fe 2p XPS Spectra and Bonding in Iron Compounds. *Surf. Interface Anal.* **2004**, *36* (12), 1564–1574.
- (58) Signorini, L.; Pasquini, L.; Savini, L.; Carboni, R.; Boscherini, F.; Bonetti, E.; Giglia, A.; Pedio, M.; Mahne, N.; Nannarone, S. Size-Dependent Oxidation in Iron/Iron-Oxide Core-Shell Nanoparticles. *Phys. Rev. B: Condens. Matter Mater. Phys.* **2003**, *68* (19), 195423.
- (59) Hasché, F.; Oezaslan, M.; Strasser, P.; Fellingner, T.-P. Electrocatalytic Hydrogen Peroxide Formation on Mesoporous Non-Metal Nitrogen-Doped Carbon Catalyst. *J. Energy Chem.* **2016**, *25* (2), 251–257.
- (60) Dembinska, B.; Brzozowska, K.; Szwed, A.; Miecznikowski, K.; Negro, E.; Di Noto, V.; Kulesza, P. J. Electrocatalytic Oxygen Reduction in Alkaline Medium at Graphene-Supported Silver-Iron Carbon Nitride Sites Generated During Thermal Decomposition of Silver Hexacyanoferrate. *Electrocatalysis* **2019**, *10* (1), 112–124.